

1 **Modelling framework for asynchronous land-atmosphere coupling using**  
2 **NASA GISS ModelE and LPJ-LMfire: Design, Application and Evaluation**  
3 **for the 2.5ka period**

4

5 Ram Singh<sup>1,2</sup>, Alexander Koch<sup>4</sup>, Allegra N LeGrande<sup>2,1</sup>, Kostas Tsigaridis<sup>1,2</sup>, Riovie D Ramos<sup>5</sup>,  
6 Francis Ludlow<sup>6</sup>, Igor Aleinov<sup>1,2</sup>, Reto Ruedy<sup>2,3</sup>, Jed O Kaplan<sup>7</sup>

7

8

9 <sup>1</sup> Center for Climate Systems Research, Columbia University, New York, USA

10 <sup>2</sup> NASA Goddard Institute for Space Studies, New York, NY-10025, USA

11 <sup>3</sup> SciSpace LLC, New York, NY, USA

12 <sup>4</sup> Department of Earth Sciences, The University of Hong Kong, Hong Kong SAR, China

13 <sup>5</sup> Earth Observatory of Singapore, Singapore

14 <sup>6</sup> Department of History, School of Histories and Humanities, Trinity College, Dublin 2, Ireland

15 <sup>7</sup> Department of Earth, Energy, and Environment, University of Calgary, Calgary AB, Canada

16

17

18 *Correspondence to:* Ram Singh ( [ram.bhari85@gmail.com](mailto:ram.bhari85@gmail.com) )

19

20 **Abstract**

21 While paleoclimate simulations have been a priority for Earth system modelers over the past  
22 three decades, little attention has been paid to the period between the mid-Holocene (6ka) and  
23 the Last Millennium, although this is an important period for the emergence of complex  
24 societies. Here, we consider the climate of 2500 BP (before present or 550 BCE), a period when  
25 compared to late preindustrial time, greenhouse gas concentrations were slightly lower, and  
26 orbital forcing led to a stronger seasonal cycle in high latitude insolation. To capture the  
27 influence of land cover on climate, we asynchronously coupled the NASA GISS ModelE Earth  
28 system model with the LPJ-LMfire dynamic global vegetation model. We simulated global  
29 climate and assessed our results in the context of independent paleoclimate reconstructions. We  
30 also explored a set of combinations of model performance parameters (bias and variability) and  
31 demonstrated their importance for the asynchronous coupling framework. The asynchronously  
32 coupled model system shows strong vegetation-albedo feedback on climate and is comparatively  
33 more sensitive to the bias correction than the internal model variability and green Sahara  
34 conditions. In the absence of a bias correction, while driving LPJ-LMfire in the coupling process,  
35 ModelE drifts towards colder conditions in the high latitudes of the Northern Hemisphere in  
36 response to land cover simulated by LPJ-LMfire. A regional precipitation response is also  
37 prominent in the various combinations of the coupled model system, with a substantial  
38 intensification of the Summer Indian Monsoon and a drying pattern over Europe. Evaluation of  
39 the simulated climate against reconstructions of temperature from multiple proxies and the  
40 isotopic composition of precipitation ( $\delta^{18}O_p$ ) from speleothems demonstrated the skill of ModelE  
41 in simulating past climate. A regional analysis of the simulated vegetation-climate response  
42 further confirmed the validity of this approach. The NASA GISS ModelE found to be  
43 particularly sensitive to the representation of shrubs and this land cover type requires particular  
44 attention as a potentially important driver of climate in regions where shrubs are abundant. Our  
45 results further demonstrate the importance of bias correction in coupled paleoclimate  
46 simulations. This study presents a generalized framework for incorporating biogeophysical  
47 responses into climate models without dynamic vegetation, for simulating past climates, in line  
48 with the recommendations of the Paleoclimate Modelling Intercomparison Project (PMIP).

Formatted: Font: 12 pt, Not Italic

Deleted: The coupled model system shows substantial vegetation albedo feedback to climate

Deleted: coupled model system

Deleted: is

Formatted: Font: Not Italic

Formatted: Font: Not Italic

## 53 **1. Introduction**

54 Earth system models (ESMs) are widely applied in paleoclimate experiments as an “out of  
55 sample” exercise to evaluate the overall quality of the model, and to better understand climate  
56 system responses to external forcings. In many paleoclimate modeling studies, it has been  
57 demonstrated that inclusion of biogeophysical and biogeochemical feedbacks between land and  
58 atmosphere feedbacks are essential to simulate the magnitude and spatial pattern of climate  
59 change that is consistent with independent reconstructions (Betts, 2000; Claussen, 1997; Cox et  
60 al., 2000; Doherty et al., 2000; Strandberg et al., 2014a). The importance of land-atmosphere  
61 feedbacks for past climate has shown particularly to be true in the context of the mid-Holocene  
62 and last glacial inception periods (Braconnot et al., 2012; Collins et al., 2017; Harrison et al.,  
63 2015; Jahn et al., 2005; Kubatzki and Claussen, 1998; Sha et al., 2019; Shanahan et al., 2015;  
64 Tierney et al., 2017). For example, for the African Humid Period of the mid-Holocene, numerous  
65 studies demonstrated that greenhouse gases (CO<sub>2</sub>, N<sub>2</sub>O, CH<sub>4</sub>) and orbital forcing are alone not  
66 sufficient for models to simulate climate that is consistent with independent paleoclimate  
67 reconstructions. The inclusion of land-atmosphere feedbacks via interactive dynamic vegetation  
68 modeling or prescribed vegetation distributions helps improves model-proxy discrepancies  
69 (Chandan and Peltier, 2020; Charney, 1975; Dallmeyer et al., 2021; Pausata et al., 2016;  
70 Rachmayani et al., 2015; Singh et al., 2023; Thompson et al., 2021; Tiwari et al., 2023;  
71 Velasquez et al., 2021). For this reason, more recent protocols (PMIP4; Otto-Bliesner et al.,  
72 2017) for simulations of the mid-Holocene specify that the land cover boundary condition should  
73 include shrub vegetation in northern Africa with greater extent than the present (the so-called  
74 “Green Sahara”), as well as an expansion of trees and shrubs at high northern latitudes.

75  
76 Instead of prescribing land cover boundary conditions in an earth system model, it may be  
77 desirable to employ a coupled model where that allows interaction between climate and  
78 vegetation. While several modern earth system models include a dynamic representation of land  
79 cover, in climate models (regional and global) that lack a coupled dynamic vegetation  
80 component a well-established technique to capture land-atmosphere feedbacks is to use  
81 asynchronous coupling. In this type of coupling, climate model output is used to drive an offline  
82 vegetation model that then returns a land cover boundary condition to the climate model.

83 To quantify the feedback between land and atmosphere and improve the fidelity of the  
84 paleoclimate simulation, asynchronous coupling typically involves running a climate model  
85 simulation for a period of a few decades, after which the mean climate state is passed to a  
86 vegetation model that in-turn produces a land cover boundary condition for the climate model.  
87 This process is repeated until climate reaches equilibrium, defined as insignificant changes in  
88 key outputs, e.g., 2m temperature, from one cycle to the next.

89  
90 (Texier et al., 1997) used the iterative asynchronous coupling between the LMD Atmospheric  
91 General Circulation Model (AGCM) and the BIOME1 vegetation model to produce an improved  
92 climate for the mid-Holocene (6ka) period and found that inclusion of land-atmosphere  
93 feedbacks led to simulations of temperatures at high latitudes and precipitation over West Africa  
94 that were more consistent with independent paleoclimate reconstructions compared to  
95 atmosphere-only simulations. (de Noblet et al., 1996) used a similar coupling to highlight the  
96 role of biogeophysical feedback in glacial initiation around 115ka ago. Asynchronous coupling  
97 has also been used with regional climate models (RCMs). (Kjellstroem et al., 2009) and  
98 Velasquez et al. (2021) both used asynchronous coupling between an RCM and land cover  
99 model to simulate the climate of Europe at the Last Glacial Maximum. Both studies  
100 demonstrated the importance of land cover in improving the agreement with reconstructions and  
101 paleoenvironmental proxies.

102  
103 This study has two objectives. First, we present a generalized design for asynchronously  
104 coupling the NASA GISS ModelE2.1 climate model (Kelley et al., 2020) with the LPJ-LMfire  
105 DGVM (Pfeiffer et al., 2013) to simulate climate including biogeophysical land-atmosphere  
106 feedbacks. Second, we demonstrate the utility of this asynchronous coupling framework for a  
107 paleoclimate period that has not been the traditional focus of paleoclimate modeling (2.5ka) and  
108 evaluate the model results against independent paleoclimate reconstructions for that period.

109  
110 2.5ka represents a time that is nearest to the present day among the different periods selected  
111 under the coordinated effort of the Paleoclimate Model Intercomparison Project (PMIP4). It is  
112 interesting because it represents an important period for the emergence of complex societies  
113 across Eurasia (Iron Age, Classical Antiquity, early Imperial China) and elsewhere. During this

Deleted:

Deleted:

116 era, favorable climate conditions around the Mediterranean might have influenced the emergence  
117 of the golden age of Greece, the Roman classical period, and other empires of the Southern  
118 Europe, North Africa, and southwest Asia (Lamb, 1982; Reale and Dirmeyer, 2000). On the  
119 other hand, adverse climate conditions due to volcanic eruptions and a series of arid phases  
120 during this period may have had a negative impact on Egyptian civilization around the Nile and  
121 Mesopotamian civilization around the Euphrates and Tigris rivers. 2.5ka is thus a key period for  
122 the study of human-environment interactions and the history of climate and society, where we  
123 may assess societal vulnerability to climate change (Ludlow and Manning, 2021; Manning et al.,  
124 2017; Mikhail, 2015; Petit-Maire and Guo, 1998; Singh et al., 2023).

125 Section 2 describes the models used in this study (Section 2.1), the initial control run for 2.5ka,  
126 and a stepwise description of the asynchronous coupling framework, including variable exchange  
127 and processing (Sections 2.2 and 2.3). Section 3 presents the experimental design for  
128 implementing the asynchronous coupled system and evaluates the PFT mapping schemes. In  
129 Section 4, we evaluate the simulated 2.5ka climate using the ModelE–LPJ asynchronous  
130 coupling framework against multi-proxy temperature reconstructions (Kaufman et al., 2020) and  
131 additionally utilized the model’s capabilities to simulate the isotopic composition of water in  
132 precipitation ( $\delta^{18}\text{O}_p$ ) to compare with the Speleothem Isotope Synthesis and Analysis (SISAL)  
133 version 2 database (Comas-Bru et al., 2020). Section 5 provides the analysis and comparison of  
134 model-simulated climate under various experimental configurations.

135

## 136 **2. Models and asynchronous coupling framework**

137 **2.1.1 NASA GISS ModelE2.1:** NASA GISS ModelE2.1 (Kelley et al., 2020), is the climate model  
138 of the NASA Goddard Institute for Space Studies (GISS) currently used in Climate Model  
139 Intercomparison Project (CMIP) phase 6 (Eyring et al., 2016). We used the NINT (Non-  
140 Interactive; physics version 1 in CMIP6) GISS ModelE2.1 version where aerosols and ozone are  
141 precomputed from the prognostic, but much more computationally demanding, chemistry and  
142 aerosols version of the model OMA (One Moment Aerosols; physics version 3 in CMIP6; (Bauer  
143 et al., 2020)). In our simulations, the GISS ModelE2.1 atmosphere has a horizontal resolution of  
144  $2^\circ \times 2.5^\circ$  (latitude/longitude) with 40 vertical layers, and the top of the atmosphere at 0.1 hPa. The  
145 ModelE2.1 atmosphere has a smooth transition from sigma layers to constant pressure layers  
146 centered at 100hPa. The atmosphere is coupled to the GISS Ocean v1 model, which runs at a

### Deleted: ¶

We evaluate the climate of 2.5 ka simulated with the ModelE-LPJ asynchronous coupling framework against multi-proxy temperature reconstructions

### Deleted: Methodology

152 resolution of 1°x1.25° (latitude/longitude) with 40 depth layers to the ocean bottom. While the  
153 biogeophysical properties of land cover are simulated with the Ent Terrestrial Biosphere Model  
154 (Ent TBM; Kiang 2012; (Kim et al., 2015)), as part of ModelE2.1 (Ito et al., 2020), Ent relies on  
155 a prescribed vegetation map and as such does not simulate changes in land cover over time. To  
156 capture the influence of climate change on land cover and biogeophysical feedbacks between land  
157 and atmosphere, asynchronous coupling with LPJ-LMfire (or any other DGVM) is currently  
158 required.

159

160 **2.1.2 LPJ-LMfire:** We used the LPJ-LMfire DGVM (v1.4.0) to simulate the land cover  
161 boundary conditions in our experiments. LPJ-LMfire (Kaplan et al., 2022; Pfeiffer et al., 2013) is  
162 an evolution of LPJ (Sitch et al., 2003) and is a process-based, large-scale representation of plant  
163 growth and decay, vegetation demographics and ecological disturbance, and water and carbon  
164 exchanges between the land and the atmosphere. LPJ-LMfire has been successfully validated for  
165 simulating present-day biogeography and fire regime characteristics, and its outputs have been  
166 compared against contemporary observations (Pfeiffer et al., 2013; Sitch et al., 2003; Thonicke  
167 et al., 2010). For this study, we simulated land cover boundary conditions at a horizontal  
168 resolution 0.5°x0.5°. LPJ-LMfire is driven by monthly fields of climate (temperature,  
169 precipitation, cloud cover, wind, and lightning), static maps of topography and soil texture, and  
170 an annual global value of atmospheric CO<sub>2</sub> concentration. LPJ-LMfire simulates land cover in  
171 the form of fractional coverages of nine plant functional types (PFTs), including tropical,  
172 temperate, and boreal trees, and tropical and extratropical herbaceous vegetation (Table 1). CO<sub>2</sub>,  
173 soil texture and topography data used to drive LPJ-LMfire are described in Pfeiffer et al. (2013,  
174 Table 3). For 2.5ka simulations, we set atmospheric CO<sub>2</sub> concentrations to 271.4 ppm (Kaplan et  
175 al., 2012). The sum of PFT fractional cover per grid box does not need to equal unity; when it is  
176 less than one the remainder is considered bare ground.

177

178 **Table 1:** - Summary of climate and PFT variables exchanged between NASA GISS ModelE and  
179 LPJ-LMfire model for asynchronous coupling process. Column 1 and 2 shows list the output and  
180 input climate variables from GISS ModelE to LPJ-LMfire models, whereas the columns 3 and 4  
181 lists the output and input plant function types (PFTs) from LPJ-LMfire to GISS ModelE.

Deleted: CO2

Formatted: Justified, Line spacing: 1.5 lines

GISS Output	LPJ-LMfire Input	Annual cycle climatology and variability (standard deviation) over the period of interest (100 Years)	LPJ-LMfire Output Vegetation (PFTs)	LPJ-LMfire to GISS ModelE (Ent) Vegetation Mapping (Vegetation cover type, Leaf area index and vegetation heights)	GISS ModelE (Ent) Vegetation (PFTs)
Surface Air Temperature (°C)	Surface Air Temperature (°C)		Tropical Broadleaf Evergreen		Evergreen Broadleaf Late Succession
Precipitation (mm/day)	Precipitation (mm/day)		Tropical Broadleaf Raingreen		Evergreen Needleleaf Late Succession
	Number of wet days				
Diurnal Surf. Air Temp Range (°C)	Diurnal Surf. Air Temp Range (°C)		Temperate Needleleaf Evergreen		Cold Deciduous Broadleaf Late Succession
Surface Wind Speed (m/sec)	Surface Wind Speed (m/sec)		Temperate Broadleaf Evergreen		Drought Deciduous Broadleaf
Moist Convective Air Mass Flux (kg/m <sup>2</sup> /sec)	Lightning Density (strokes/Km <sup>2</sup> /day)		Temperate Broadleaf Summergreen		Deciduous Needleleaf
			Boreal Needleleaf Evergreen		Cold Adapted Shrub
			Boreal Summergreen		Arid Adapted Shrub
			C3 Perennial Grass		C3 Grass Perennial
		C4 Perennial Grass	C4 Grass		
			C3 Grass Annual		
			Arctic C3 Grass		
			Bright Bare Soil		
			Dark Bare Soil		

185  
 186 **2.2. 2.5ka Simulation setup (Initial control run using ModelE)**  
 187 We started the 2.5ka and preindustrial (PI) control experiments following the PMIP4 and CMIP6  
 188 protocols (Eyring et al., 2016; Kageyama et al., 2018). The PI simulation uses preindustrial (year  
 189 1850) GHG concentrations and a modern continental configuration and serves as the reference  
 190 experiment for designing the boundary conditions for past time slices studied in PMIP4. GHG and  
 191 orbital forcings for the preindustrial (PI) control experiment correspond to levels observed in  
 192 1850 CE (CO<sub>2</sub>: 284 ppm, N<sub>2</sub>O: 273 ppb, CH<sub>4</sub>: 808 ppb). For the 2.5ka control experiment, orbital  
 193 parameters (Berger et al., 2006) were specified for 2,500 years BP (before present ~550 BCE), and  
 194 greenhouse gas CO<sub>2</sub>, N<sub>2</sub>O, and CH<sub>4</sub> were set to ~279 ppm, ~266 ppb, and 610 ppb respectively  
 195 (Köhler et al., 2017; Loulergue et al., 2008; Otto-Bliesner et al., 2017; Schneider et al., 2013;  
 196 Siegenthaler et al., 2005). We considered only natural emissions as sources of aerosols in the  
 197 atmosphere, zeroing-out any anthropogenic contribution to aerosol and aerosol precursors. For  
 198 biomass burning, in the absence of any better estimate, we assumed that the emissions provided  
 199 by CEDS (Hoesly et al., 2018) for the year 1750 are all natural. Land cover consists of the  
 200 fractional coverages of 13 plant functional types (PFTs) and includes vegetation height and leaf  
 201 area index (LAI). For the PI and initial (0<sup>th</sup> order) simulations, land cover type and monthly-  
 202 varying LAI were derived from satellite (MODIS) data (Gao et al., 2008; Kattge et al., 2011;  
 203 Myneni et al., 2002; Tian et al., 2002a, b; Yang et al., 2006) and vegetation heights from (Simard  
 204 et al., 2011). We also used the mid-Holocene (6k) vegetation under PMIP4 protocol, which is  
 205 linearly interpolated to 2.5ka period and details of vegetation cover changes (Singh et al., 2023;  
 206 Figure S1) and associated impacts on the northern hemisphere climate due to the inclusion of  
 207 scaled PMIP4 vegetation using the interactive chemistry version of NASA GISS ModelE2.1  
 208 (MATRIX) are discussed in (Singh et al., 2023).

210 **2.3 Asynchronous coupling framework**

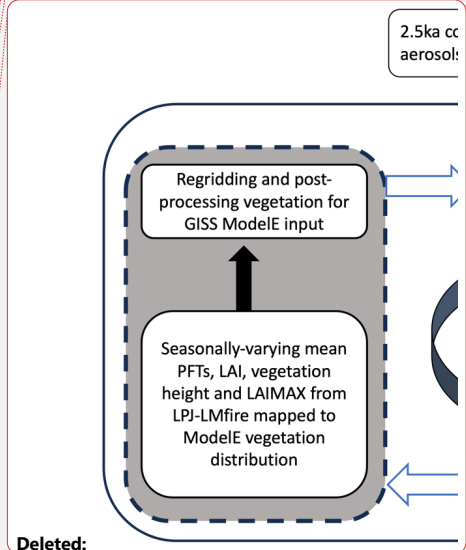
211 The asynchronous coupling between ModelE and LPJ-LMfire is summarized in Figure 1. For each  
 212 iteration, ModelE simulated climate is used by LPJ-LMfire, which, returns the PFT fractional  
 213 cover, LAI, and vegetation height that are used as boundary conditions for the next ModelE  
 214 simulation.

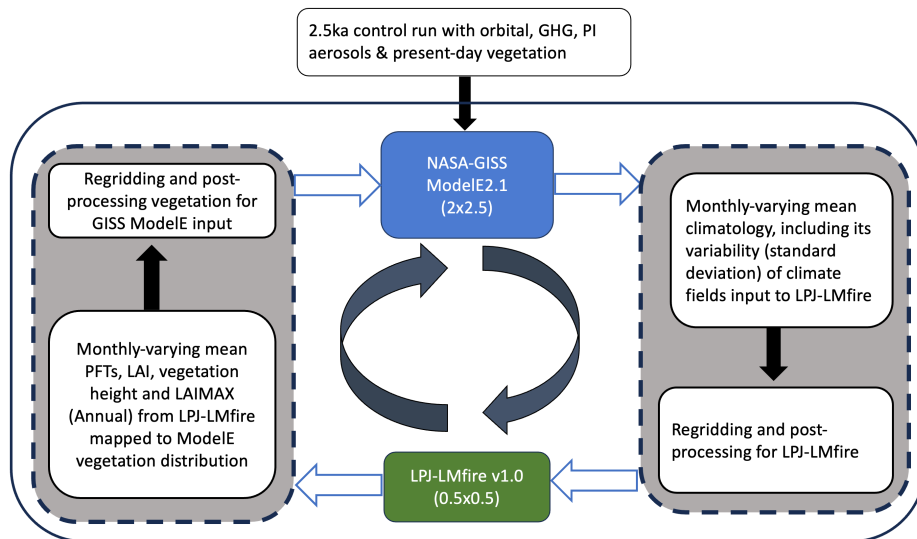
**Deleted: Table 1:** - Summary of climate and PFT variables exchanged between NASA GISS ModelE and LPJ-LMfire model for asynchronous coupling process. Column 1 and 2 shows lists the output and input climate variables from GISS ModelE to LPJ-LMfire models, whereas the columns 3 and 4 lists the output and input plant function types (PFTs) from LPJ-LMfire to GISS ModelE. ¶

**Deleted:**

**Deleted: C**

**Deleted: F**





227  
 228 Figure 1: Flow diagram for the asynchronous coupling [framework](#) between GISS ModelE2.1 and  
 229 LPJ-LMfire models. For the climate fields input to LPJ-LMfire refer to (Table 1, Column 1) and  
 230 LPJ-LMfire PFTs (Table 1, Column 3)

231  
 232 **2.3.1 GISS ModelE2.1 simulations:** Climatological monthly mean climate (Table 1, Column 1)  
 233 for a 100-year period were extracted from a well equilibrated ModelE simulation. To assess  
 234 interannual variability with monthly resolution, we calculated the standard deviation of the decadal  
 235 mean data for each month across the 100-year equilibrium period.

236 **2.3.2. LPJ-LMfire simulations:** All climate variables except diurnal temperature range, wet days,  
 237 and lightning density were provided directly from the ModelE output. For derived climate  
 238 variables, the additional processing steps are described below.

239  
 240 Diurnal temperature range was calculated as the difference of the monthly-mean daily maximum  
 241 and minimum temperatures as simulated by ModelE. Wet days were calculated from modelled  
 242 precipitation based on an empirical relationship between present-day monthly total precipitation  
 243 and the number of wet days per month. To quantify this relationship, we performed a nonlinear  
 244 regression between monthly total precipitation and number of days with measurable precipitation

245 using the CRU TS 4.0 gridded climate fields (Harris et al., 2020). Using those data, we developed  
246 a set of regression coefficients for every land gridcell that allowed us to estimate wet days for any  
247 paleoclimate period based only on monthly total precipitation. Lightning density was estimated  
248 based on modelled convective mass flux following Magi (2015). However, the feedback to climate  
249 due to fire-driven emissions are not included, as accounting for them would require active  
250 atmospheric chemistry and transport, which are not included in LPJ-LMfire.

**Formatted:** Font: 12 pt, Not Italic

**Deleted:** Lightning density was estimated based on modelled convective mass flux following

**Formatted:** Font: 12 pt, Not Italic

**Deleted:**

251  
252 Because LPJ-LMfire requires a timeseries of interannually varying climate forcing to run, we  
253 processed the climatological monthly mean climate produced by the ModelE for use with the  
254 vegetation model. In brief, ModelE climate was converted into anomalies by differencing the  
255 paleoclimate simulation with ModelE simulated climate for the late 20<sup>th</sup> century (1951-2000). The  
256 resulting climate anomalies were bilinearly interpolated to a 0.5°x0.5° grid and added to a baseline  
257 climate based on observations over 1951-2000. The resulting climatology was expanded to a 1020-  
258 year-long time series by adding interannual variability in the form of detrended and randomized  
259 climate anomalies from the 20<sup>th</sup> Century Reanalysis (Compo et al., 2011). LPJ requires climate  
260 input data with interannual variability because fires and other disturbance events occur only in  
261 years with anomalous climate, for example, hot or dry years Sitch et al. (2003). Driving the model  
262 with climatological mean climate will result in disturbance frequencies that are lower than the  
263 expected mean that in some regions would lead to an overabundance of tree cover when we would  
264 expect herbaceous vegetation. For further details on this process, see (Hamilton et al., 2018).

**Formatted:** Font: 12 pt, Not Italic

265 Because LPJ-LMfire is computationally inexpensive, we ran each simulation for 1020 years.  
266 While the composition and characteristics of aboveground vegetation comes into equilibrium with  
267 climate after a few centuries of simulation, a millennium-long simulation brings the terrestrial  
268 carbon pools into equilibrium as well. The land cover boundary conditions returned to the climate  
269 model represent the mean modeled vegetation cover over the final 250 years of the LPJ-LMfire  
270 simulation.

271  
272 **2.3.3. LPJ-LMfire to GISS ModelE vegetation mapping:** LPJ-LMfire simulates land cover in  
273 the form of nine PFTs, while in GISS ModelE the vegetation component (Ent TBM) recognizes  
274 13 PFTs. We mapped the LPJ-LMfire generated PFT cover, LAI, LAIMAX, and vegetation height

278 to the GISS ModelE2.1 (Ent) PFTs in order to feed it to the ModelE (Table 1, Column 3 & 4). The  
279 main points for the LPJ-LMfire to GISS vegetation mapping are the following:

280

281 - Early and late-successional PFTs were approximated from the LPJ-LMfire output using  
282 the model simulated fire frequency and monthly burned area fraction. High fire frequency  
283 favors early-successional PFTs because the time between disturbances is shorter than that  
284 required for establishment. By definition, late-successional PFTs require extended periods  
285 of low disturbance to persist within the ecosystem. However, because successional state is  
286 indistinguishable in the satellite-driven reference vegetation for the historical period used  
287 as the boundary condition for ModelE, we combined early & late successional PFTs in our  
288 simulations.

289 - LPJ-LMfire does not have a specific PFT for shrubs (arid and cold), while Ent does. To  
290 estimate shrub cover in LPJ-LMfire, we used LPJ-LMfire simulated tree height for the  
291 tropical broadleaf raingreen, temperate broadleaf summergreen, and boreal summergreen  
292 PFTs and specified that trees with height lower than a globally-uniform predefined  
293 threshold were considered to be shrubs (Table S1).

294 - Ent has an Arctic grass PFT while LPJ-LMfire does not. To estimate Arctic grass cover we  
295 used the C<sub>3</sub> grass PFT in LPJ-LMfire and specified it as Arctic grass in regions where the  
296 boreal summergreen PFT was also present. LPJ-LMfire also does not distinguish between  
297 annual and perennial grasses, and so to map these to Ent we assumed that these were  
298 present in equal fractions among the simulated C<sub>3</sub> grass in the LPJ-LMfire simulation.

299 - The non-vegetated fraction of a grid cell is assigned to the bare soil, and the distribution of  
300 bright and dark soil color heterogeneity is classified/redistributed based on the present-day  
301 structure of soils over a grid cell.

302

303 Of particular importance to our coupled model simulations was that the PFTs simulated by LPJ-  
304 LMfire do not explicitly include a shrub type. To approximately distinguish tree from shrub cover,  
305 we generated three LPJ-to-GISS mapping schemes that differed on how shrubs are specified. A  
306 set of possible changes in various PFT classifications are adopted based on the comparison with  
307 GISS vegetation distribution and categorized the mapping methodologies. These mappings,  
308 summarized in table S1, differ in the height threshold of trees to be re-categorized as cold and arid

Formatted: Font: 12 pt, Not Italic

Deleted:

Deleted: shrub

Deleted:

312 shrubs, and the fraction of perennial grass re-categorized into perennial and arctic grasses. Also,  
313 the monthly leaf area index (LAI) and vegetation height readjusted using the weighted mean for  
314 remapped LPJ-LMfire vegetation PFTs.

315  
316 **2.3.4. Step 4. Post-processing of vegetation files:** LPJ-LMfire model generates output at a  
317 horizontal resolution of 0.5°x0.5°. We resampled the output vegetation information to the  
318 2.0°x2.5° grid used by ModelE2.1. In a few cases, land cover extrapolated using a nearest-neighbor  
319 approach was to cover all the gridcells identified as land in the ModelE standard land-sea mask.

320

### 321 **3 Experimental Design**

322 Apart from evaluating the framework for the PI control period, we designed a set of experiments  
323 to evaluate various aspects of the simulated climate, including model bias, and variability in both  
324 the climate, and vegetation models. For example, one known limitation in the current version of  
325 ModelE is a wintertime cold bias over the Arctic in simulations covering the historical period  
326 (Kelley et al., 2020).

327

328 Table 2 shows the combinations of the model metrics selected to explore the utility of the  
329 asynchronous coupling framework and their impact on simulated climate. Run names are  
330 designated using Time (1850, 2.5k), Vegetation source (PI, GS), Bias Correction (BC) and  
331 Interannual Variability (LPJ, GISS) separated by “\_”. For example, ‘1850\_PI\_ctrl’ and  
332 ‘2.5k\_PI\_ctrl’ denote the 1000-year-long PI and 2.5k runs with GISS PI vegetation. GS stands for  
333 Green Sahara and PI = Pre-Industrial. An “x” denotes the absence of a particular criterion (default  
334 state). Run ‘1850\_PI\_ctrl’ (row 1 in table 2) was performed to evaluate the vegetation mapping  
335 scheme and to select the appropriate scheme for asynchronous coupling, whereas ‘2.5k\_PI\_ctrl’  
336 (row 2 in table 2) is used as the 0<sup>th</sup> order control run for 2.5ka period with present-day vegetation  
337 distribution. Runs ‘2.5k\_PI\_BC\_LPJ’, ‘2.5k\_PI\_x\_x’, and ‘2.5k\_PI\_x\_GISS’ are three branches  
338 extended from ‘2.5k\_PI\_ctrl’ with the combinations of bias correction and interannual variability  
339 from LPJ and GISS models. For the ‘2.5k\_GS\_x\_GISS’ and ‘2.5k\_GS\_BC\_GISS’ simulations,  
340 we initialized the land cover boundary conditions to approximate 2.5ka by linearly interpolating  
341 cover fractions between the 6ka land cover prescribed under the PMIP4 protocol (Otto-Bliesner et  
342 al., 2017) and the PI reference dataset and extended the 0<sup>th</sup> order 2.k control (‘2.5k\_PI\_ctrl’) before

Deleted:

Formatted: Justified, Line spacing: 1.5 lines

Formatted: Superscript

Deleted:

Deleted:

Formatted: Superscript

346 branching out the experiments '2.5k\_GS\_x\_GISS' and '2.5k\_GS\_BC\_GISS'. Details of the 6ka  
347 land cover boundary conditions under for PMIP4 and associated impacts on Northern Hemisphere  
348 climate using the interactive chemistry version of NASA GISS ModelE2.1 (MATRIX) are  
349 discussed by (Singh et al., 2023). Model equilibrium is determined using the threshold that the  
350 absolute value of the decadal-mean planetary radiative imbalance must be  $< 0.2 \text{ W m}^{-2}$ , along with  
351 the surface temperature trend (absolute value  $< 0.1 \text{ }^\circ\text{C}/50 \text{ years}$ ). Convergence across iterations is  
352 evaluated by comparing the annual mean climate state and vegetation distributions between  
353 successive iterations.

Deleted:

Formatted: Font: Not Italic

Formatted: Font: Not Italic

Deleted: ¶

Formatted: Font: Not Bold

356 **Table 2:** - Summary of experiment designs followed to explore and evaluate the GISS ModelE -  
 357 LPJ-LMFire model asynchronous coupling framework. See text for an explanation on the run  
 358 naming convention.

Run Name	Initial Vegetation Cover	Bias correction	Interannual Variability	Number of Iterations/total number of years	Remark
1850_PI_ctrl	Used to evaluate the LPJ to GISS vegetation mapping schemes <u>GHG Forcing: CO<sub>2</sub>: 284 ppm, N<sub>2</sub>O: 273 ppb, CH<sub>4</sub>: 808 ppb</u>				
2.5k_PI_ctrl	1000-year-long control; base run to branch out the other simulations <u>GHG Forcing: CO<sub>2</sub>: 279 ppm, N<sub>2</sub>O: 266 ppb, and CH<sub>4</sub>: 610 ppb</u>				
2.5k_PI_BC_LPJ	GISS PI vegetation	YES	LPJ	5/750 years	converged
2.5k_PI_x_x	GISS PI vegetation	No	No	2/270 years	Too cold in 3 <sup>rd</sup> iteration diverging
2.5k_PI_x_GISS	GISS PI vegetation	No	GISS ModelE (100years)	4/550 years	Too cold diverging
2.5k_GS_x_GISS	GISS PI vegetation + Green Sahara+ Boreal Forest	No	GISS ModelE (100years)	5/1150 years	Too cold diverging
2.5k_GS_BC_GISS	GISS PI vegetation + Green Sahara+ Boreal Forest	YES	GISS ModelE (100years)	4/1000 years	converged

359 \* Convergence means the final model simulation has a similar climatology with the previous  
 360 iteration, whereas divergence means the model is drifting away from the expected states.

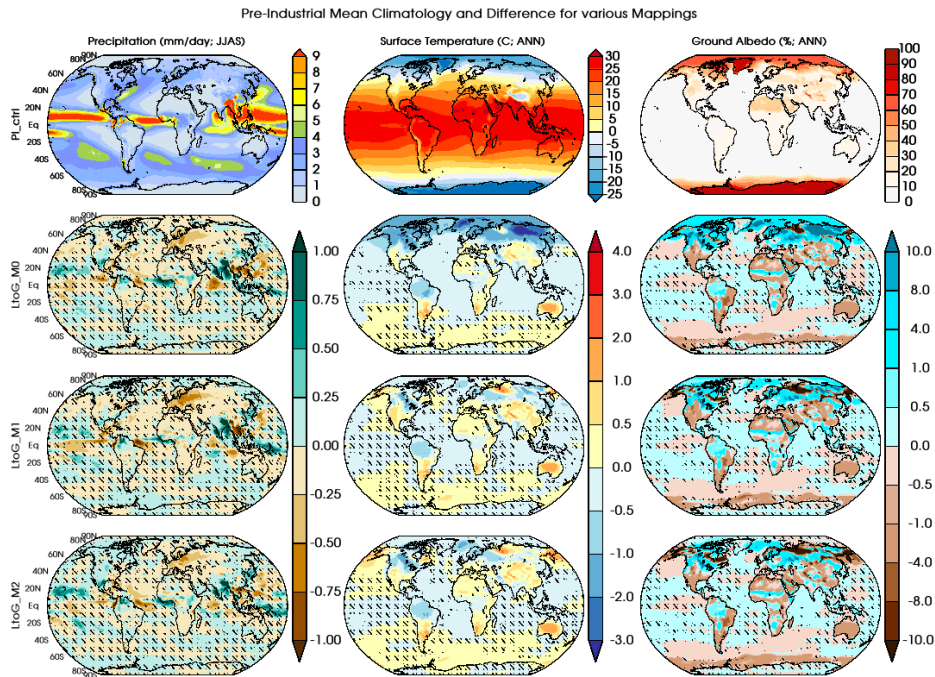
361

362

363 **3.1 Evaluation & Validation of LPJ-GISS Mapping Methodologies**

364 We used the standard present-day land cover boundary conditions described for ModelE2.1  
365 (Kelley et al., 2020) for the initial 0<sup>th</sup>-order iteration of the pre-industrial and 2.5ka control  
366 climate simulations. This land cover dataset is based on satellite observations (Gao et al., 2008;  
367 Myneni et al., 2002; Tian et al., 2002a, 2002b; Yang et al., 2006) from the Moderate Resolution  
368 Imaging Spectroradiometer (MODIS), with leaf area index (LAI) from the TRY database (Kattge  
369 et al. 2011), and vegetation height (Simard et al. 2011) from the Geoscience Laser Altimeter  
370 System (GLAS). Branches of the 2.5ka run for green Sahara conditions are started using the  
371 linearly interpolated vegetations for 2.5ka from the 6ka vegetation distribution defined based on  
372 the PMIP4 protocol (Otto-Bliesner et al., 2017; Singh et al., 2023). These land cover boundary  
373 conditions are shown as the fractional coverage of 13 PFTs (including bare soils) (Figs. S1.A and  
374 S1.B). In these figures, bare dark and bare bright are merged into a single bare soil fractional  
375 cover.

376  
377 The ModelE2.1 pre-industrial (PI) control run initialized with the present-day land cover boundary  
378 condition is processed through the asynchronous coupling framework to evaluate the mapping  
379 scheme for converting LPJ PFTs to GISS (Ent) PFTs. We tested three sets of LPJ-to-GISS  
380 mapping schemes as required in the asynchronous coupling framework. Differences among the  
381 mapping schemes are described in supplementary table TS1. Three parallel control runs are  
382 performed for 100 years, each initialized with the vegetation distribution that corresponds to the  
383 corresponding mapping scheme and compared to the mean climate state of the parent PI control  
384 run.  
385



386  
 387 **Figure 2.** Comparison of seasonal mean climate metrics when using different vegetation mapping  
 388 schemes with that of the original PI control. Top row shows the mean climatology for precipitation  
 389 (mm/day; JJAS), surface air temperature (°C; ANN) and ground albedo (%; ANN) and row 2 to 4  
 390 shows the differences in mean climate for the mappings LtoG\_M0, LtoG\_M1 and LtoG\_M2,  
 391 respectively. Stippling indicates the region over which change is not statistically significant at a  
 392 95% confidence interval (Used the student's t-test).

393  
 394 The mapping schemes LtoG\_M1 and LtoG\_M2 (supplementary table TS1) generate a similar  
 395 spatial structure of annual surface air temperature with broadly similar regional characteristics  
 396 (Fig. 2). A shift towards colder climates of 2-3 °C in mean annual temperature over the higher  
 397 latitudes of the Northern hemisphere is simulated when using the mapping scheme LtoG\_M0,  
 398 which is not present when using the other mapping schemes (LtoG\_M1 and LtoG\_M2). We  
 399 selected forests into shrubs to match the missing PFTs in ModelE vegetation distributions based  
 400 upon the tree height (Table S1). In these mapping schemes, the fraction of boreal tree PFTs

401 assigned to cold shrubs depends on simulated tree height, which is, in turn, influenced by surface  
402 temperature (Bonan, 2008; Bonan et al., 1992; Li et al., 2013; Thomas and Rowntree, 1992). In  
403 the mapping LtoG\_M0, the fractional cover of boreal tree PFTs was reduced significantly,  
404 leading to an increase in ground albedo (up to 10%), which led to the model drifting towards  
405 comparatively colder climate conditions. When using the other two mapping schemes (LtoG\_M1  
406 and LtoG\_M2) the assignment of boreal tree PFTs to shrub types is limited by a higher tree  
407 height threshold and partially because other PFTs (perennial grass) are substituted for cold  
408 shrubs. Regional patches of increased ground albedo and surface cooling over the higher  
409 latitudes of the Northern Hemisphere are also evident when using the LtoG\_M1 and LtoG\_M2  
410 translation schemes.

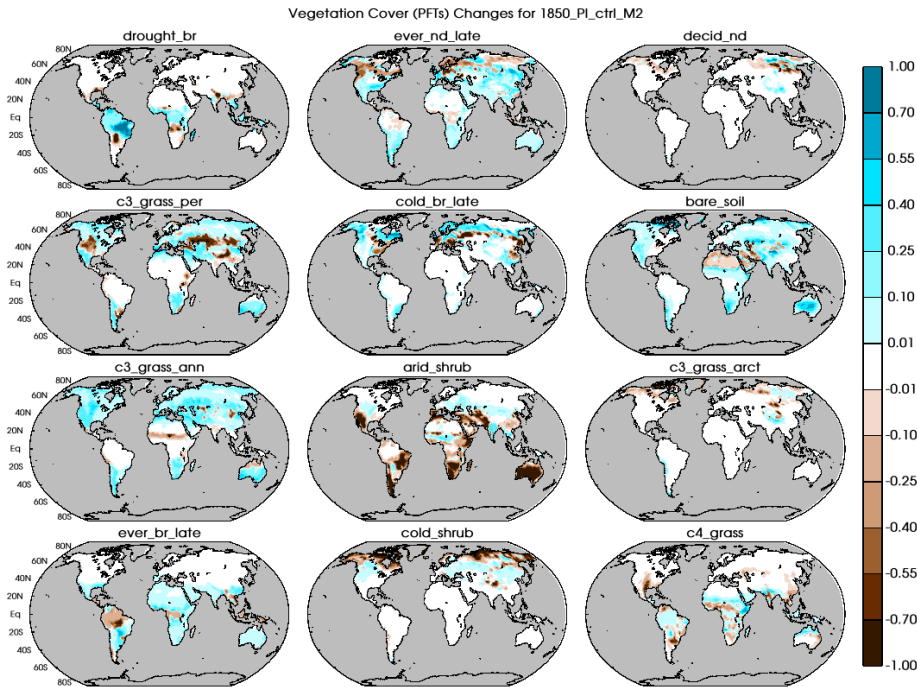
411  
412 Precipitation during the Northern Hemisphere summer monsoon season (JJAS; June-July-  
413 August-September) appears similar among the three mapping schemes, as the larger changes are  
414 confined to the equatorial regions. A drying pattern over Europe appears in all three translation  
415 schemes, but it is comparatively more substantial under LtoG\_M0 and LtoG\_M1 than LtoG\_M2.

416  
417 All translation schemes also lead to increased precipitation over equatorial South America.  
418 Annual mean river runoff for the Amazon River is simulated at 305, 297, and 308 km<sup>3</sup>/month for  
419 LtoG\_M0, LtoG\_M1 and LtoG\_M2, respectively, a slight improvement to the original  
420 Preindustrial (PI) run runoff of 280 km<sup>3</sup>/month with using the standard present-day land cover  
421 boundary condition. Compared to observations, ModelE2.1 shows a substantial deficit in  
422 Amazon River runoff in present-day simulations because of insufficient precipitation over the  
423 watershed (Fekete et al., 2001; Kelley et al., 2020).

424  
425 Based on this evaluation of the different ways of translating LPJ PFTs to GISS PFTs, we found  
426 that LtoG\_M2 was the scheme that simulates global precipitation and surface temperature most  
427 consistent with observations, and ground albedo that is closest to the standard pre-industrial  
428 boundary conditions dataset used usually used to drive ModelE. Figure 3 shows the difference in  
429 PFT cover fraction using LPJ-LMfire with the LtoG\_M2 scheme compared to the standard  
430 ModelE boundary condition land cover data set for the late preindustrial time (PI; 1850 CE).

**Deleted:** (Thomas and Rowntree, 1992; Bonan et al., 1992; 2008; Li et al., 2013)

433 Compared to the ModelE standard land cover dataset for PI, LPJ-LMfire simulates increased  
 434 extent and fraction of most trees (drought broadleaf, evergreen needleleaf, and evergreen  
 435 broadleaf). Despite selecting a relatively high threshold for tree height to be classified as shrubs  
 436 (up to 11 meters for both arid and cold types) the simulated cover fraction of shrubs is low  
 437 compared to the standard PI land cover dataset for ModelE. The coverage of both annual and  
 438 perennial C<sub>3</sub> grasses is greater in LPJ-LMfire in extratropical and polar regions, similarly, C<sub>4</sub>  
 439 grasses, which are not present in cooler climates, shows greater coverage in LPJ-LMfire in  
 440 equatorial regions. LPJ-LMfire simulates some vegetation cover in the Sahara and Arabian  
 441 deserts while the standard PI boundary conditions dataset suggests that most of this region is  
 442 bare soil.



443  
 444 **Figure 3.** Differences between the LPJ-LMfire simulated vegetation distribution (PFTs and land  
 445 cover type) and satellite-based land cover boundary conditions used in ModelE for PI control  
 446 period and the selected mapping schemes (LtoG M2).

447

Deleted: ¶

Deleted: under

450 **3.3 Vegetation Cover Changes under various combinations**

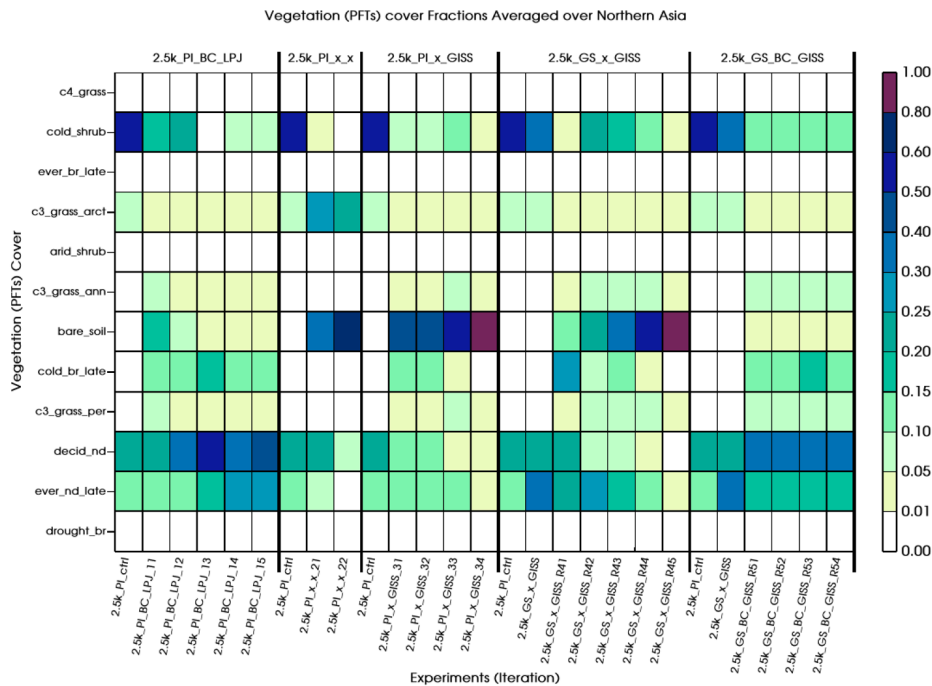
451 We chose a set of five model configurations (Table 2) to quantify the model bias and interannual  
452 variability in our asynchronous coupling framework for the 2.5ka period. Figures S2.A, S2.B,  
453 S2.C, S2D, and S2.E show the spatial differences between prescribed land cover boundary  
454 conditions maps and land cover interactively simulated by our LPJ-LMfire-ModelE coupled  
455 model, which is henceforth referred to as the “coupled model system”. These land cover  
456 difference maps are shown for each of the different model configurations described above,  
457 following the final iteration of the asynchronous coupling when the coupled model system is  
458 assumed to be either equilibrated or the process was truncated due to instability (Table 2).  
459 Figures S2.A, S2.B, and S2.C show the changes in the land cover from the default ModelE land  
460 cover boundary conditions map for PI (Fig S1.A); Figures S2.D and S2.E show the differences  
461 calculated from the modified vegetation following the PMIP4 protocols (Fig S1.B).

462  
463 Across all configurations, most of the tree PFTs show an increase in cover in the coupled model  
464 system relative to the prescribed land cover maps. However, in simulations where bias correction  
465 to the climate model was not applied, deciduous needleleaf tree cover is reduced in the high  
466 latitudes of the Northern Hemisphere (2.5k\_PI\_x\_x, 2.5k\_PI\_x\_GISS and 2.5k\_GS\_x\_GISS)  
467 and this, in turn, has a substantial impact on regional climate. The coupled model system  
468 simulates increased annual and perennial C<sub>3</sub> grass cover across all configurations relative to the  
469 prescribed maps, while the Arctic C<sub>3</sub> grass shows a mixed regional response. Increased C<sub>4</sub> grass  
470 cover is mostly confined to the equatorial region and Southern Hemisphere; over the Northern  
471 Hemisphere C<sub>4</sub> grass cover decreases, irrespective of the inclusion and exclusion of interannual  
472 variability or bias correction. As discussed previously, the extent of arid and cold shrubs is  
473 reduced significantly in the coupled model system relative to the prescribed maps, even when the  
474 threshold height to separate trees shrubs was set at a relatively tall limit of 11 m. A similar  
475 reduction in shrub cover relative to the land cover map used to initialize the simulation  
476 vegetation distributions is also simulated under all configurations.

477  
478 In Figures 4 and 5 we present heatmap-type diagrams of the mean land cover fraction over  
479 selected regions to demonstrate and understand the pattern of change in vegetation distribution  
480 simulated by the coupled model system. These figures depict changes in land cover under the

481 different asynchronous coupling experimental configurations used in this study. Vegetation  
 482 fraction changes averaged over northern Asia (NAS) (Fig. 4) and eastern Africa (Fig. 5; see Fig.  
 483 13 for the region boundaries; NAS: magenta; EAF: blue). Deciduous needleleaf tree cover over  
 484 northern Asia (60°N-77°N, 70°E-135°E) is replaced by bare soil in all experimental  
 485 configurations where bias correction of the climate model output was not applied. A similar  
 486 disappearance of evergreen needleleaf late-successional forests, as well as a quick disappearance  
 487 (within the first iteration) of cold shrubs, was also noticed. This suggests that, in the absence of  
 488 bias correction the model's drift towards colder conditions strongly influences vegetation growth  
 489 in subsequent iterations over higher latitudes, which is inconsistent with the standard land cover  
 490 boundary condition dataset used with ModeLE (Kelley et al., 2020). On the other hand, when bias  
 491 correction is applied along with interannual variability from either model (2.5K\_PI\_BC\_LPJ and  
 492 2.5K\_GS\_BC\_GISS), boreal forests are present in the northern Asia region along with cold  
 493 shrubs and grasses.  
 494

Deleted: 9

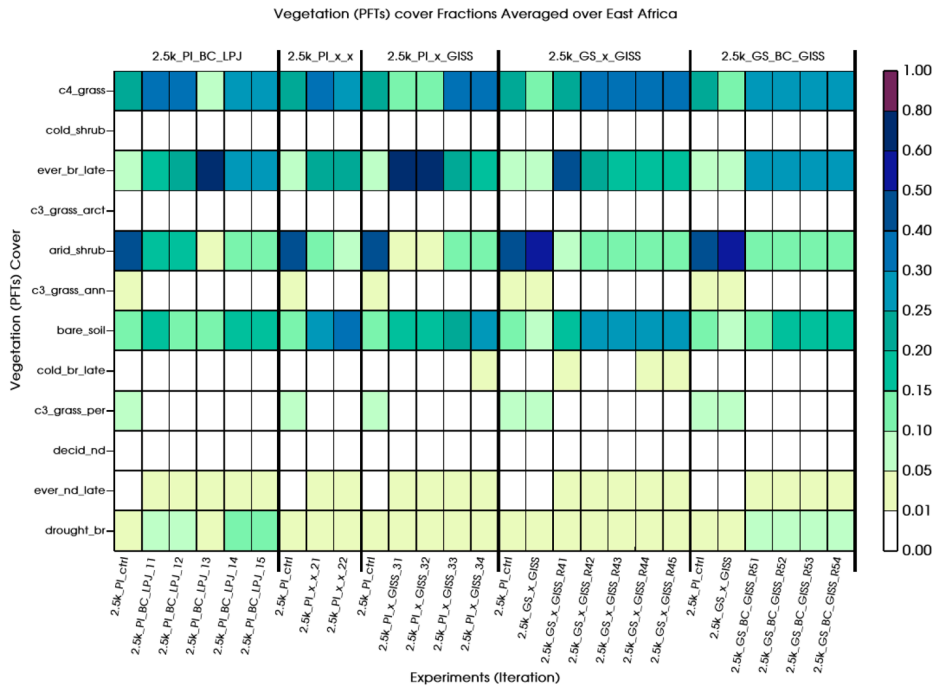


497 Figure 4. Area average of fractional land cover over Northern Asia region (60°N-77°N, 70°E-  
 498 135°E) under the range of experimental configurations used in this study.

499

500 Over eastern Africa (EAF: 0° N-18° N, 25° E-46° E) the impact of bias correction is less  
 501 important than over the high latitudes of the Northern Hemisphere. The presence of broadleaf  
 502 tree PFTs (drought broadleaf and evergreen broadleaf) and C<sub>4</sub> grasses is consistent across all the  
 503 experimental configurations we used. However, the cover fraction arid shrubs decreased  
 504 substantially, associated with a slight increase in the bare soil fraction.

505



506

507 Figure 5. Same as Figure 4A, but for Eastern Africa (0°N-18°N, 25°E-46°E).

508

509 **4.0 Comparison with paleoclimate-proxy records for 2.5ka**

Deleted: c

Deleted: 5

512 To evaluate the coupled model system's skill in representing past climate, we compared our  
513 simulations for 2.5ka with multiproxy temperature reconstructions and speleothem-based oxygen  
514 isotope records.

515

#### 516 4.1 Comparisons with reconstructed temperature

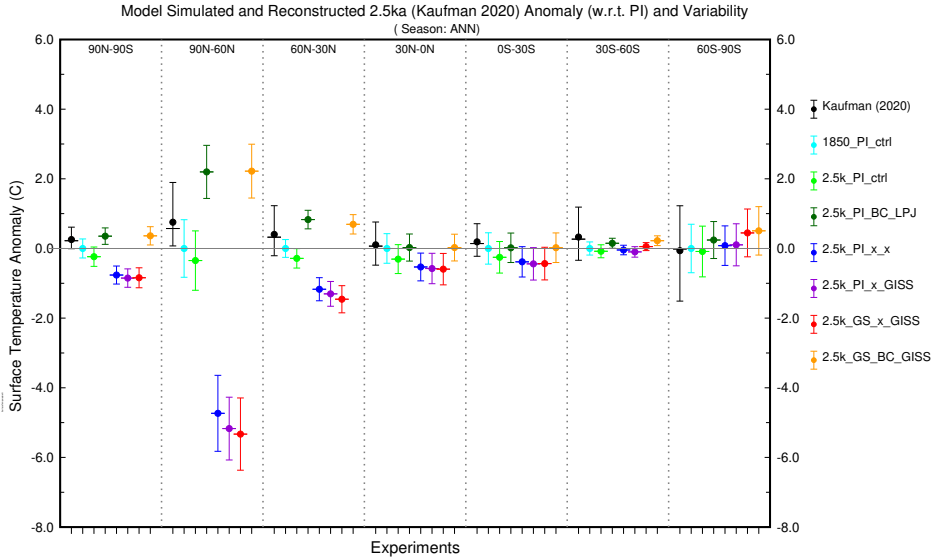
517 Kaufman et al. (2020) used five different statistical methods to reconstruct temperature at 1319  
518 globally distributed sites covering part or all of Holocene from a range of proxy types. For each  
519 method, a 500-member ensemble of plausible reconstructions was presented. For comparison  
520 with our model output, we extracted temperature anomalies for 2.5ka (relative to the value  
521 reconstructed for the late preindustrial Holocene) from the ensemble reconstructions which we  
522 binned into six latitude bands between the North and South Poles (each 30 degrees wide). We  
523 computed the mean and median zonal anomaly using all 500 estimates of mean surface  
524 temperature (MST) over each band for each of the five methodologies (total 2500), along with  
525 the 5-95 percentile interval to represent uncertainty/variability among the sites in the zone and  
526 across reconstruction methods (black bar in Figure 6) as suggested (Kaufman et al. 2020).

Deleted: ¶

Formatted: Left

Deleted: 12

Deleted: ¶



527

533 Figure 6: Comparison of model-simulated annual surface temperature anomalies and interannual  
534 variability for 2.5ka (with LPJ-LMfire vegetation) against the independent proxy-based  
535 temperature reconstructions (black, Kaufman et al., 2020). Mean (circle), median (line) along with  
536 5-95 percentile range as variability bars (whiskers) and different colors represent the final iteration  
537 of our different experiments.

Deleted: 12

539 It shows that the 2.5ka control simulation with present-day vegetation is comparable to pre-  
540 industrial conditions (1850\_PI\_ctrl), exhibiting a slightly cooler climate. In contrast, proxy-based  
541 surface temperature reconstructions (Kaufman et al., 2020) indicate slightly warmer conditions at  
542 global mean as well as across most latitude bands, except the far south (60S-90S). Applying bias  
543 correction allows the model to reproduce the same anomaly sign as the reconstruction, with  
544 minimal global (90N-90S) mean bias relative to the proxy data (2.5k\_PI\_BC\_LPJ and  
545 2.5k\_GS\_BC\_GISS). Although the magnitude of warming remains higher at the northern  
546 hemisphere high latitudes, this framework demonstrates the improved capability of the model to  
547 reproduce reconstructions via incorporating biogeophysical effects of past vegetation by  
548 adopting a bias correction. Model simulations where bias correction was not applied show colder  
549 conditions than the reconstructions globally and in the Northern Hemisphere. These differences  
550 between model and proxy are very large in the high latitudes of the Northern Hemisphere and  
551 statistically significant throughout the extra-tropics. In the Southern Hemisphere, the differences  
552 between model and proxy reconstructions are smaller and insignificant, and there is less  
553 difference between simulations with and without bias correction. It should be noted that the  
554 larger uncertainty in reconstructed temperature over the southern polar band is due to a  
555 noticeably lower number of available proxy records (157 records; Kaufman et al., 2020).

Formatted: Font: Not Italic

Deleted: It shows that the 2.5ka control simulation with present-day vegetation is comparable to pre-industrial conditions (1850\_PI\_ctrl), exhibiting a slightly cooler climate. In contrast, proxy-based surface temperature reconstructions (Kaufman et al., 2020) indicate slightly warmer conditions at global mean as well as across most latitude bands, except the far south (60S-90S). Applying bias correction allows the model to reproduce the same anomaly sign as the reconstruction, with minimal global (90N-90S) mean bias relative to the proxy data (2.5k\_PI\_BC\_LPJ and 2.5k\_GS\_BC\_GISS). Although the magnitude of warming remains higher at the northern hemisphere high latitudes, this framework demonstrates the improved capability of the model to reproduce reconstructions via incorporating biogeophysical effects of past vegetation by adopting a bias correction

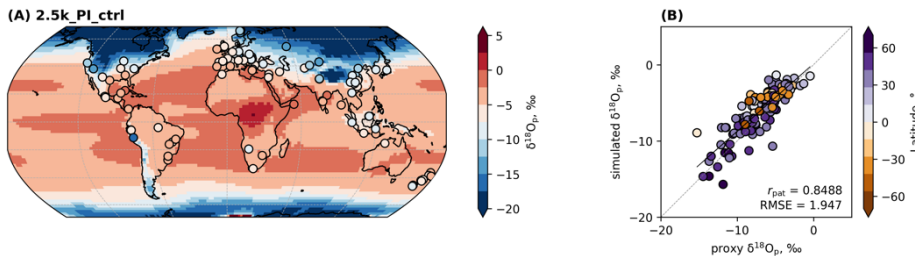
#### 557 **4.2 Comparisons with speleothem oxygen isotope ratios**

Deleted: 5

558 The isotopic composition of oxygen in water, expressed as the ratio of  $^{18}\text{O}$  to  $^{16}\text{O}$  serves as a  
559 fundamental tracer for investigating changes in the hydrological cycle. This ratio is highly  
560 sensitive to regional climate conditions and to the processes that regulate the hydrological cycle,  
561 such as temperature, precipitation, and evaporation. ModelE2.1 includes a representation of the  
562 stable water isotopologues as passive tracers and the isotopic composition of precipitation can be  
563 diagnosed from the model output (Aleinov and Schmidt, 2006; LeGrande and Schmidt, 2006;

582 Schmidt, 1998). We compared the simulated mean annual isotopic composition of precipitation  
 583 ( $\delta^{18}\text{O}_p$ ) with oxygen isotope records from the Speleothem Isotope Synthesis and Analysis  
 584 (SISAL) version 2 database (Comas-Bru et al., 2020). Using the published chronologies for each  
 585 speleothem record we extracted all samples dated between 3-2 ka, which resulted in 163  
 586 measurements from 111 sites. Depending on their mineralogy (i.e., calcite or aragonite), the  
 587 mean  $\delta^{18}\text{O}$  values (VPDB) were converted to their drip water equivalents that could be compared  
 588 to simulated  $\delta^{18}\text{O}_p$  (VSMOW) (Comas-Bru et al., 2020). We used simulated mean surface air  
 589 temperature obtained from the grid points nearest each cave sites to estimate the cave  
 590 temperature required to convert mineral  $\delta^{18}\text{O}$  to an equivalent the drip water value. For each of  
 591 our model experiments, we extracted simulated  $\delta^{18}\text{O}_p$  nearest to each cave site and compared it  
 592 with the estimated drip-water  $\delta^{18}\text{O}$ .

593 Overall, the mean  $\delta^{18}\text{O}_p$  spatial distribution in all 2.5ka simulations is in excellent agreement  
 594 with the proxies, showing better pattern correlations ( $r_{pat}$ ) than 0.83 (Figure 7), with  
 595 the 2.5k\_PI\_x\_x iteration marginally showing the highest skill (i.e.,  $r_{pat} = 0.85$  and RMSE =  
 596 1.90; shown in supplementary Fig S4). For comparison, the worst simulation using this metric,  
 597 2.5k\_GS\_BC\_GISS, is almost as equally skillful ( $r_{pat} = 0.84$  and RMSE = 1.92; Fig. S4),  
 598 demonstrating that none of the different configurations we presented here were significantly  
 599 different.



600  
 601 Figure 7. Comparison of simulated  $\delta^{18}\text{O}_p$  with speleothem  $\delta^{18}\text{O}$ . Left: global distribution (70° S-  
 602 70° N) of simulated  $\delta^{18}\text{O}_p$  (background) and speleothem  $\delta^{18}\text{O}$  (circles), converted to their drip  
 603 water equivalents (see text) for the 2.5k\_PI\_ctrl simulation. Right: scatterplots between simulated  
 604 and proxy  $\delta^{18}\text{O}_p$ . Black line represents the least squares regression fits to data points while the gray  
 605 dashed line represents the 1:1 line.  $r_{pat}$  and RMSE are reported in the lower right corner of the  
 606 scatterplot. For comparison against each model experiment, see Fig. S4

Deleted: 13

Deleted: 13

609

610 Regionally, we similarly found that most simulations show no significant deviation with each  
611 other (Figure 8, Figure 9). We note, however, that over Europe (Figure 9E), variability may be  
612 explained by the observed change in magnitude on both SAT and summer precipitation among  
613 simulations (further sections). Over India and Central Asia (Figure 9F), simulations with bias  
614 correction show lower correlation and higher RMSE values compared to other models against  
615 proxy  $\delta^{18}\text{O}_p$ . This is likely related to the observed increase in mean summer precipitation over  
616 this region that were not reflected in the proxy sites.

617

618 Compared to proxy  $\delta^{18}\text{O}_p$ , simulations over certain regions show better agreement. Europe,  
619 which is the most densely sampled region, show the best agreement with the proxies (i.e., high  
620 correlation, closest to the reference point, Figure 9E) with the 2.5k\_PI x\_GISS iteration best  
621 capturing the spatial  $\delta^{18}\text{O}_p$  pattern (i.e.,  $r_{pat} = 0.94$  and  $\text{RMSE} = 1.26$ ). In contrast, simulations  
622 over Central America, South America and Africa show the least skill where the magnitude of  
623  $\delta^{18}\text{O}_p$  change are consistently underestimated (i.e., moderate to high correlation but farthest away  
624 from the reference point). This may largely be due to inadequate sampling in these regions,  
625 especially for Africa, and/or both precipitation and SAT influencing  $\delta^{18}\text{O}$  may be underestimated  
626 at these proxy locations, resulting in a generally muted  $\delta^{18}\text{O}$  response across simulations. Cave-  
627 specific factors that alter speleothem  $\delta^{18}\text{O}$  (e.g., groundwater mixing, fractionation, (Baker et al.,  
628 2019; Hartmann and Baker, 2017; Lachniet, 2009) are also not effectively reproduced in the  
629 models, contributing to the proxy-model mismatch. Regions where the largest simulated SAT,  
630 precipitation, and  $\delta^{18}\text{O}_p$  change relative to the 2.5k\_PI\_ctrl are observed, such as northern Africa,  
631 the Amazon basin and Siberia, are not adequately represented by reconstructions, highlighting  
632 the need to expand the proxy network to marine-based records and polar regions over the period  
633 of interest to capture the full range of isotopic variation.

Deleted: 14

Deleted: 15

Deleted: 15

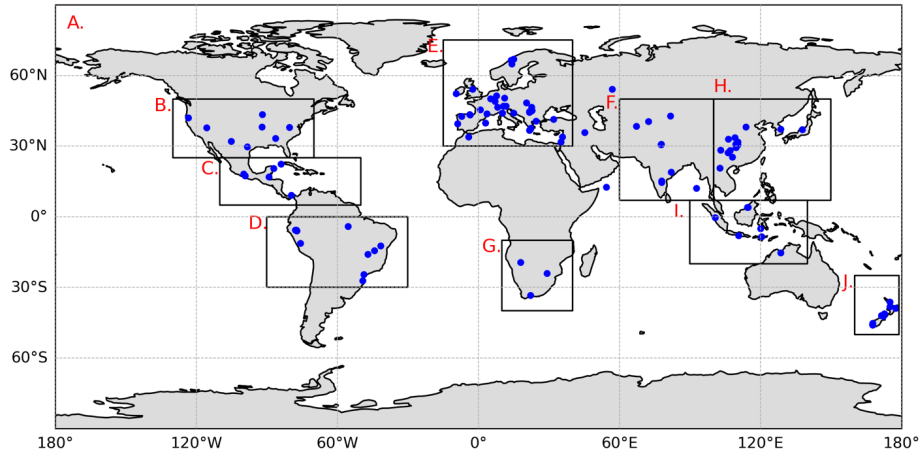
Deleted: F

Deleted: figure 7, 8, 10

Deleted: 15

Deleted: (Figure 10)

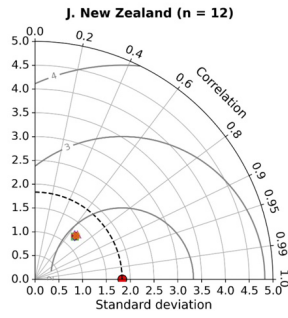
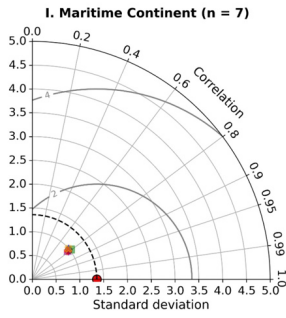
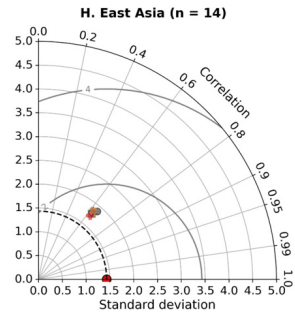
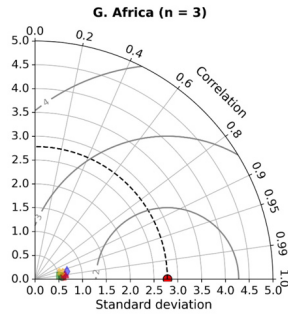
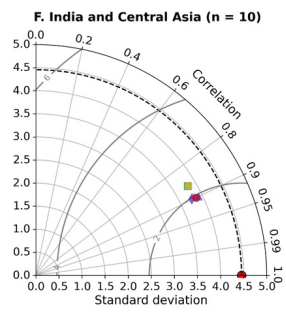
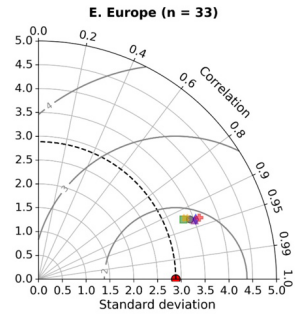
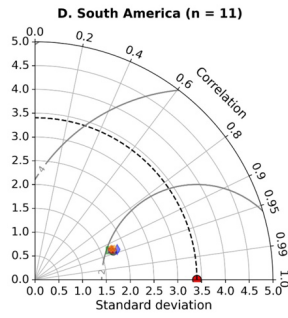
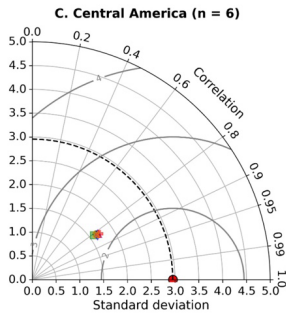
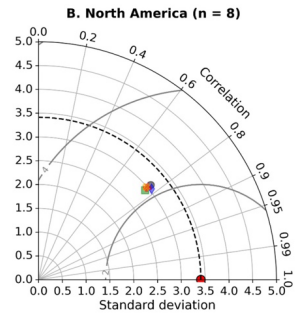
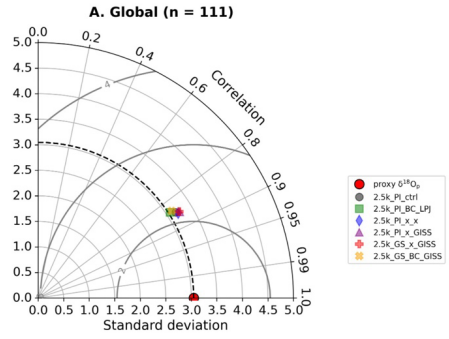
Deleted: 15



642  
 643 Figure 8. Demarcation of each geographical region. Labels A to J correspond to the respective  
 644 Taylor diagram plots in Figure 9.

Deleted: 14

Deleted: 15



648 Figure 9. Taylor diagrams showing the r, SD and RMSE values between the proxy-derived and  
649 simulated  $\delta^{18}\text{O}_p$  for each 2.5k iteration globally (A) and at each subregion (B to J). Subregions are  
650 demarcated in supporting figure 8.

Deleted: 15

Deleted: 14

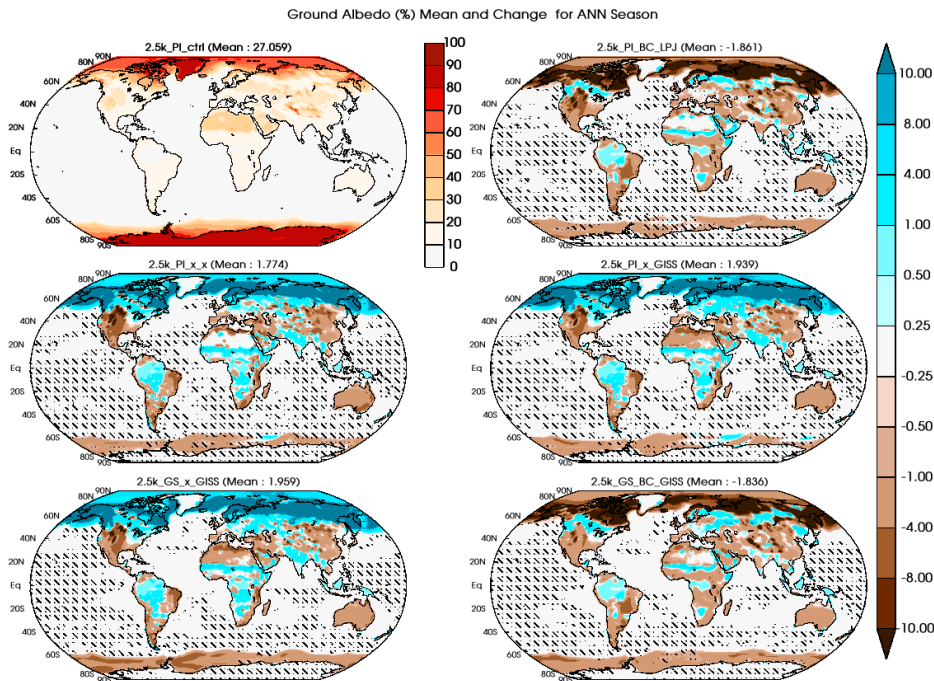
### 653 5.0 Global climate response

Deleted: 4

654 To evaluate the spatial features of the equilibrium climate simulated by ModelE, we analyzed the  
655 last 100 years of the final iteration of each coupled model system experimental configuration. We  
656 aimed to understand the biogeophysical feedback due to vegetation cover changes as well as the  
657 role of model configuration on climate. Figure 10 shows surface albedo (%) for ModelE in its  
658 initial PI state, and differences between this initial state and simulated albedo for 2.5ka using the  
659 coupled model system. We used student's t-tests to estimate if the albedo differences were  
660 statistically significant at 95% confidence interval. The coupled model system shows substantial  
661 vegetation cover change over the high latitudes of the Northern Hemisphere. As expected, most of  
662 the significant changes occur over land, while changes in albedo over the oceans are largely  
663 insignificant. The spatial pattern of albedo change differs between simulations where bias  
664 correction was applied (2.5k\_PI\_BC\_LPJ and 2.5k\_GS\_BC\_GISS) and those where it was not  
665 (2.5k\_PI\_x\_x, 2.5k\_PI\_x\_GISS, and 2.5k\_GS\_x\_GISS). Albedo over the high latitudes of the  
666 Northern Hemisphere decreases up to 10% caused by increased tree cover fraction (deciduous  
667 needleleaf and evergreen needleleaf) in the coupled model system relative to standard PI land  
668 cover dataset.

Deleted: 6

669



674  
 675 Figure 10. Annual mean (top left; 2.5k PI ctrl) and change (all other panels) of surface albedo  
 676 (%) for the final iteration of various experiment configurations listed in Table 2. Stippling indicates  
 677 the region over which change is not statistically significant at a 95% confidence interval (Used the  
 678 student's t-test).

679  
 680 This increased tree cover fraction subsequently absorbs more incoming solar radiation and raises  
 681 surface temperature by 2-4 °C over high latitude regions compared to the control run (Fig. 11,  
 682 top-right and bottom-right panels). In experiments where bias correction was not applied  
 683 (2.5k\_PI\_x\_x, 2.5k\_PI\_x\_GISS and 2.5k\_GS\_x\_GISS), the relatively cold conditions simulated  
 684 by the coupled model system shows an opposite albedo-vegetation response (> 3 °C cooling over  
 685 Northern Hemisphere high latitudes). This drift towards a colder climate in the absence of bias  
 686 correction resulted in the continuous formation of sea ice that ultimately reaches the (shallow)  
 687 seabed, effectively creating land ice and eliminating the ocean from the grid cell. In coupled  
 688 model system experiments without bias correction, we terminated the iterative processes when

Deleted: 6

Deleted: in

Deleted: 7

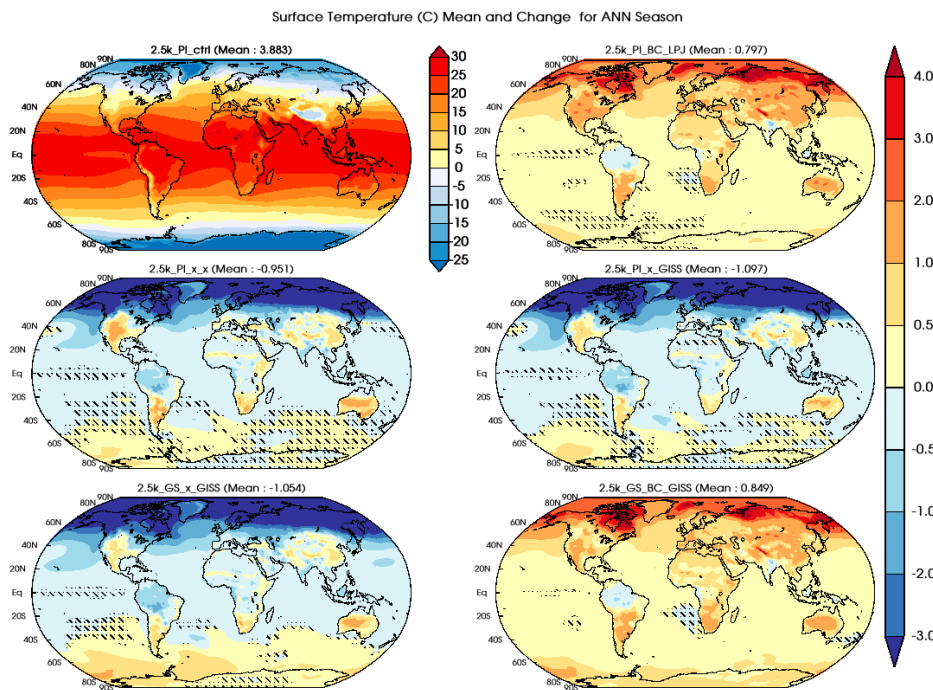
Deleted: strong

Deleted: gridcell

694 this freezing of the ocean to the seabed occurred, because this condition caused the model to  
695 crash (2.5k\_PI\_x\_x, 2.5k\_PI\_x\_GISS, and 2.5k\_GS\_x\_GISS).

696  
697 At lower latitudes, albedo tends to show decreases relative to the standard boundary conditions  
698 in all experiments, particularly over the forested areas of the equatorial regions and temperate  
699 latitudes of the Northern Hemisphere. Over the northern Africa and the Indian subcontinent  
700 changes in both albedo and surface temperature are more mixed. Albedo change in central and  
701 northern Africa driven by a reduction in the area occupied by shrubs and an increase in bare soil  
702 fraction. This pattern of increased albedo is more prevalent in simulations that were initialized  
703 with Green Sahara land cover boundary conditions.

704



705  
706 Figure 11. Same as figure 10 for Surface air temperature (°C) mean and change on an annual scale  
707 (ANN season).

708

Deleted: 7

Deleted: 6

711 In experiments that were initialized with “Green Sahara” land cover boundary conditions where  
712 interannual variability from GISS ModelE is included with and without adopting the bias  
713 correction, comparison of the surface temperature response between simulations with  
714 (2.5k\_GS\_x\_GISS; Figure 11, bottom-left) and without bias correction (2.5k\_GS\_BC\_GISS;  
715 Figure 11, bottom-right) reveal the significance of bias correction for the asynchronous coupling  
716 process. Broadly, we can observe that bias correction induces a warming of 0.7-0.8 °C, and  
717 exclusion leads to a cooling of 0.9-1.1 °C, at the global scale, predominantly over the northern  
718 hemisphere land regions.

719

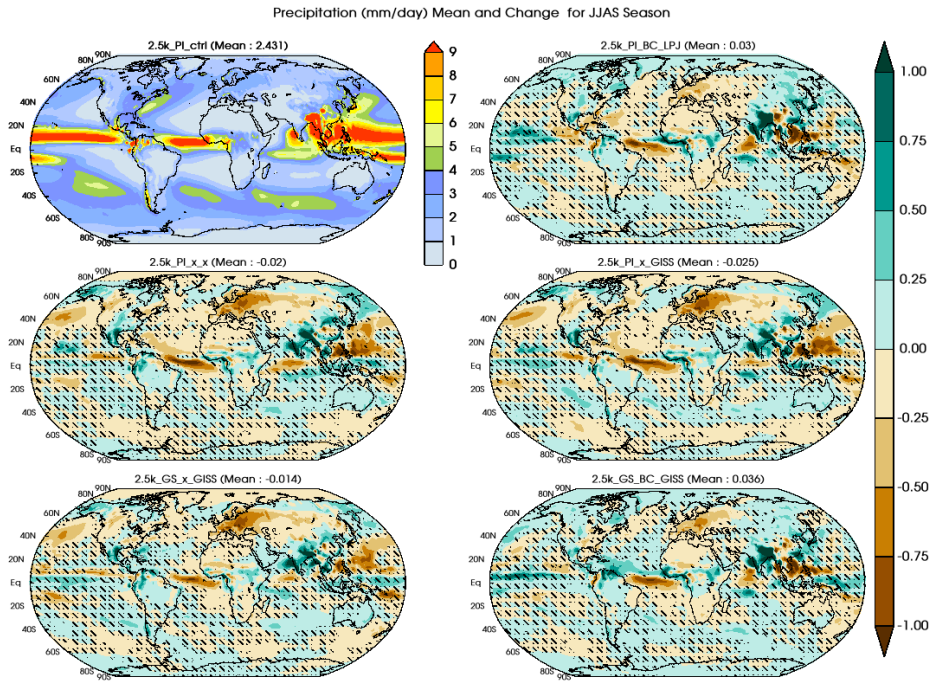
720 Precipitation change across the model configurations is shown for Northern Hemisphere summer  
721 (JJAS) at global scale in Figure 12. The significance of bias correction is noticeable over the  
722 high latitudes of the Northern Hemisphere. Simulations with bias correction (2.5k\_PI\_BC\_LPJ,  
723 2.5k\_GS\_BC\_GISS) lead to an increase in JJAS season precipitation relative to the initial  
724 boundary conditions, while those experiments without bias correction (2.5k\_PI\_x\_x,  
725 2.5k\_PI\_x\_GISS) show reductions in precipitation. Reductions in precipitation relative to initial  
726 conditions are visible in Europe in all configurations and are greater in experiments where bias  
727 correction was not applied. Another common feature among the experiments was the variable  
728 spatial pattern of JJAS precipitation change over tropical regions. All configurations showed  
729 increased precipitation over south and east Asia. Over the Nile headwaters in East Africa  
730 (Melesse et al., 2011) precipitation increased, particularly in those experiments where bias  
731 correction was applied. Interestingly, increased Northern Hemisphere summer monsoon  
732 precipitation season (JJAS) over the Asian continent was simulated across all configurations. In  
733 contrast, only a marginal northward procession of ITCZ over tropical Africa was simulated.

734

Deleted: 7

Deleted: 7

Deleted: 8



738

739

740 Figure 12. Same as figure 10 for precipitation (mm/day) mean and change for the JJAS season.

741

### 742 5.1 Regional climate

743 The spatial pattern of changes in climatic features for 2.5ka using our coupled model system  
 744 shows several prominent and robust regional signatures of climate change. We selected nine  
 745 regions over land (Fig. 13; Table 3) to analyze regional temperature and precipitation changes in  
 746 our simulations. Area-averaged time-series anomalies with respect to the 2.5ka control run  
 747 (2.5k\_PI\_ctrl) for the various experiments performed are calculated for these different regions.

748

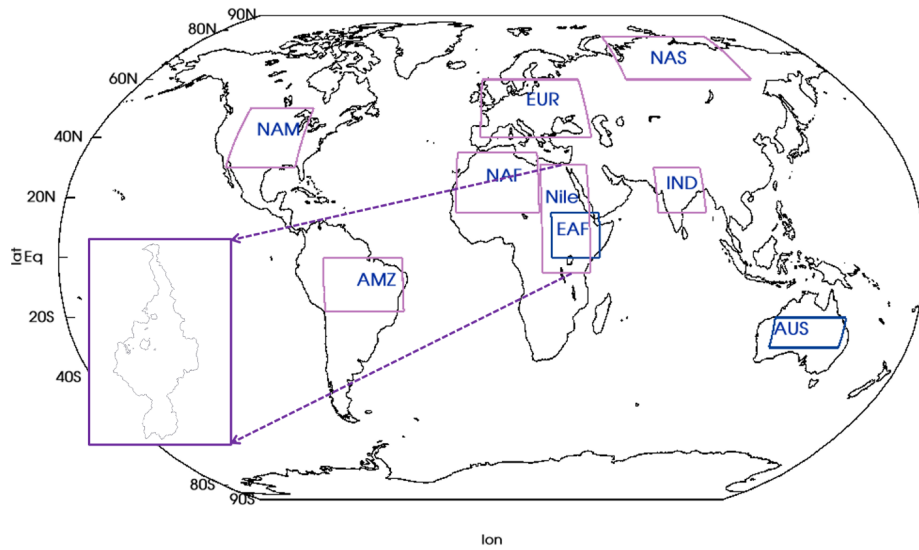
Deleted: 8

Deleted: 6

Deleted: on an annual scale (JJAS season).

Deleted: 4

Deleted: 9



754  
755  
756  
757  
758  
759  
760  
761

Figure 13. Boundaries for the regions used for regional analysis. The inset map shows the Nile River basin in high resolution, which is superimposed upon the ModelE resolution to generate the grid-specific weights for the Nile River basin. The EAF and AUS regions are used in Figs. 4 and 15.

Deleted: 9  
Deleted: A  
Deleted: I

765 **Table 3:** - Regions details including the boundary co-ordinates for all the regions.

Region (long name)	Region (short name)	Region boundary (Latitudes)	Region boundary (Longitudes)
North America	NAM	30°-50° N	115°-85° W
Amazon Rainforest Region	AMZ	0°-18° S	37°-70° W
Northern Asia	NAS	60°-77° N	70°-135° E
North Africa	NAF	15°-35° N	15° W-20° E
Europe	EUR	40°-60° N	5° W-45° E
Indian Region	IND	15°-30° N	70°-90° E
Nile River Basin	Nile	5° S-31° N	21°-41° E
East Africa	EAF	5°-15° N	25°-45° E
Australia	AUS	20°-30° S	120°-150° E

Deleted: (Siberia)

766

767

768 Figure 14 shows box-and-whisker plots of mean and median annual surface temperature (top)  
 769 and JJAS seasonal precipitation (bottom) change, as well as the 5-95 percentile range  
 770 (interannual variability) along with the upper and lower quartiles (25<sup>th</sup> and 75<sup>th</sup> percentiles) of the  
 771 anomaly time series for each region. As suggested from the global analyses of spatial patterns,  
 772 the shift towards relatively warmer or colder climate as a result of applying bias correction is  
 773 evident. Bias correction leads to pronounced warming over northern Asia (NAS region) of 3-4  
 774 °C, while without bias correction this region cools by 5-6 °C. The partition between experiments  
 775 with and without bias correction is also apparent over selected regions of the mid-latitudes  
 776 between 35°-60° N (NAS and EUP).

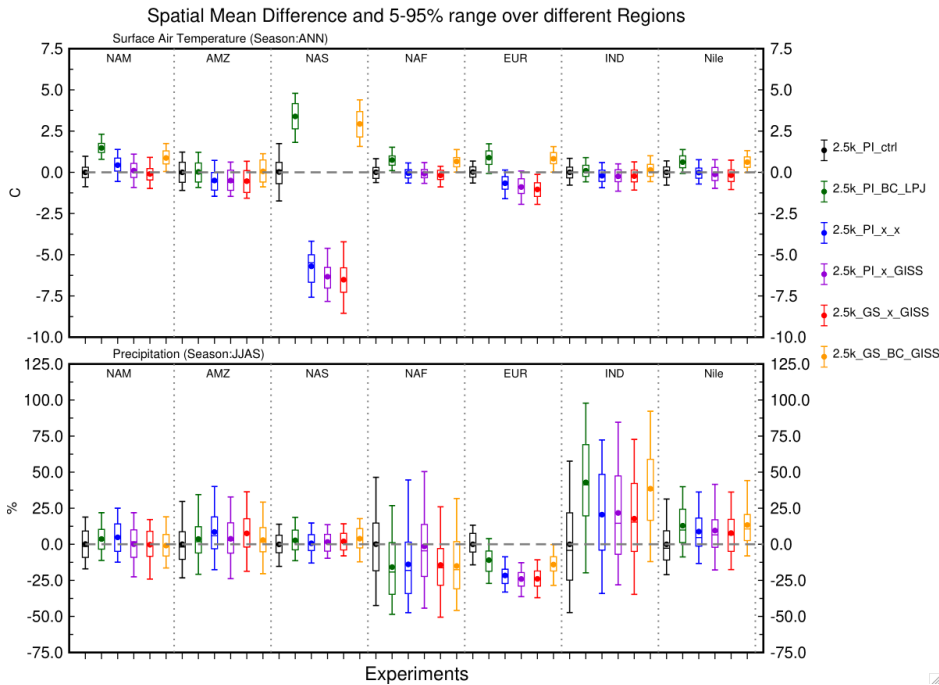
Deleted: 0

777

778 Except for northern Asia (NAS), all regions show approximately similar interannual variability  
 779 in mean annual surface temperature. In northern Asia interannual variability is greater, especially  
 780 in simulations where bias correction was not applied. Our results show that interannual  
 781 variability in summer temperature in northern Asia is sensitive to changes in land cover, with  
 782 greater variability in simulations where bias correction was not applied.

Deleted: strong

786



787

788 Figure 14. Regional change in surface air temperature (top panel, °C, annual mean) and  
789 precipitation (bottom panel, %, JJAS) for the various simulations with respect to the 2.5ka control  
790 run (2.5k\_PI\_ctrl). Regions name as listed in table 3.

791

792 Simulated 2.5ka precipitation for the Northern Hemisphere summer (JJAS) shows substantial  
793 changes in mean state relative to the 2.5ka control with PI vegetations, particularly for the  
794 tropical regions of northern Africa, India, and the Nile basin (Fig. 14, bottom panel). Interannual  
795 variability in precipitation is comparable to the initial control run (black line). However, the  
796 magnitude of variability differs across the regions; it is more prominent in tropical regions than  
797 in the extratropic. An increase in mean precipitation of order of 20-30% without bias correction  
798 and up to 40% with bias correction is simulated in JJAS season precipitation for the Indian  
799 summer monsoon region (IND and it is in a range of 10-25% increase over the Nile basin region.  
800 A drying pattern over Europe (EUR) ranges from 10-25% and is consistent for all the

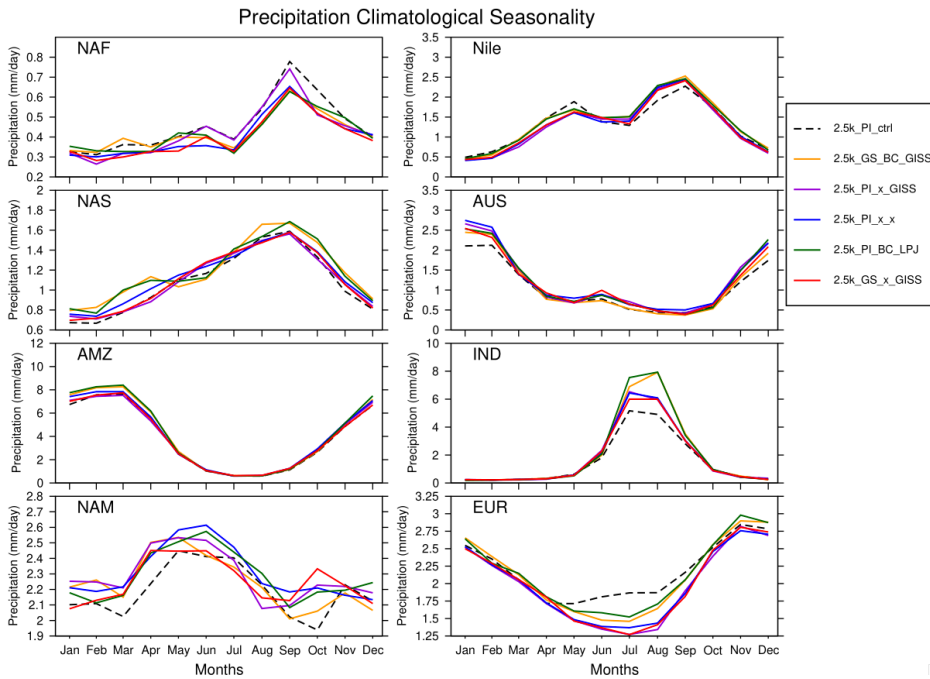
Deleted: 0

Deleted: 0

Deleted: extratropics

804 simulations; a greater decrease in European precipitation was simulated when bias correction is  
805 not adopted. A similar drying pattern was also simulated over the North America (NAM) and  
806 northern Africa (NAF) regions. The relatively small magnitude of interannual variability in  
807 precipitation over Europe and North America suggests that model does not produce high  
808 variability across these regions and that it is not sensitive to the different experimental  
809 configurations. Despite the large changes in both mean state and variability in temperature,  
810 precipitation over northern Asia (NAS) changes little from the control state and across  
811 simulations. In the Amazon region (AMZ), precipitation changes were small and not  
812 significantly different between simulations. Without bias correction, the coupled model system  
813 suggests a modest increase in mean seasonal precipitation up to 10%. We also noticed a similar  
814 response of slightly increased precipitation in Southern Hemisphere summer (DJF) over  
815 Australia (not shown here).

816  
817 We further investigated the way our experiments influenced the seasonal cycle of temperature  
818 and precipitation over the regions discussed above. Our results show that the seasonal cycle of  
819 surface temperature is broadly similar across experiments for all the equatorial regions except the  
820 Amazon (AMZ) region, where surface temperature is reduced by 0.5 °C in experiments where  
821 bias correction was not applied (Fig. S3). Over the northern Asia (NAS) region, we see a  
822 considerable difference in the seasonal cycle of temperature of 5-15 °C between runs with and  
823 without bias correction. The seasonal cycle of temperature in the 2.5ka control (2.5k\_PI\_ctrl)  
824 simulation over NAS is intermediate to the experiments but tracks closer to the simulations  
825 where bias correction was applied, particularly in Northern Hemisphere winter, where, as noted  
826 above, simulations without bias correction result in very cold conditions in this region.  
827



828  
 829 Figure 15. Seasonality of precipitation averaged over the selected regions for the final iteration of  
 830 each experiment listed in table 2.

831  
 832 Compared to temperature, the seasonal cycle of precipitation shows greater differences among  
 833 simulations over several of the regions (Fig. 15). An increase of 2-3 mm/day over the Indian  
 834 region (IND) is simulated during the Indian Summer Monsoon months (JJAS) when using LPJ-  
 835 LMfire-generated land cover for both types of experiments (with and without bias correction),  
 836 with the bias-corrected simulations showing a larger increase in precipitation than the non-bias-  
 837 corrected ones. When bias correction is applied, the seasonal peak of precipitation shifts from  
 838 July to August. Over Europe, we observe a decrease of up to 0.5 mm/day in summer  
 839 precipitation relative to the control simulation in all simulations that use the LPJ-LMfire PFTs.  
 840 Precipitation decreases even more when the bias correction was not applied. The North Africa  
 841 region (NAF) also shows a slight decrease in precipitation relative to the control over most of the  
 842 seasonal cycle, while in North America (NAM) we see an increase in precipitation outside of the  
 843 JJAS summer months. The Amazon rainforest region (AMZ) shows no change in the seasonal

Deleted: 1

Deleted: 1

846 cycle of precipitation in all experiments. The Nile River basin (Nile) and Australian (AUS)  
847 regions also show small increases in precipitation relative to the control in their respective  
848 monsoon seasons (JJAS and DJF). Overall, the changes in annual precipitation cycle (increases  
849 or decreases) over the regions are primarily driven by both the pole-equator thermal gradients in  
850 the various experiments, as well as the biogeophysical effects associated with regional vegetation  
851 changes over these regions (e.g. Indian Summer monsoon, North American and European  
852 region) (Pausata et al., 2014; Tiwari et al., 2023; Singh et al., 2023).

Formatted: Font: 12 pt

## 854 6.0 Discussion and Conclusions

855 Here we presented a generalized technical framework for asynchronously coupling a climate  
856 model (NASA GISS ModelE2.1) with a dynamic vegetation model (LPJ-LMfire) i.e., the “coupled  
857 model system”, and demonstrate its skill in reconstructing climate in the late preindustrial  
858 Holocene and for 2.5ka. We examined the role of bias and interannual variability corrections in  
859 this process, and showed how they influence simulated land cover and climate. We demonstrated  
860 the importance of considering such metrics in such a framework in our experimental design and  
861 global and regional scale analyses. We performed a detailed evaluation and comparison of the  
862 climate simulated by the coupled model system with reconstructions of air temperature (Kaufman  
863 et al., 2020) and the isotopic composition of precipitation ( $\delta^{18}\text{O}_p$ ) based on speleothems (Comas-  
864 Bru et al., 2020). Similarly to previous studies that used asynchronous coupling to simulate  
865 regional and global paleoclimate (Claussen\*, 2009; Kjellstrom et al., 2009; de Noblet et al., 1996;  
866 Strandberg et al., 2011, 2014b; Texier et al., 1997; Velasquez et al., 2021), we assessed the  
867 influence of the biogeophysical feedback between land and atmosphere.

Deleted: ( Kjellstrom et al., 2008; Texier et al., 1997; Noblet et al., 1997; Velasquez et al., 2021; Claussen, 2009; Strandberg et al., 2011, 2014)

868 Our results demonstrate the pronounced influence of including bias correction when passing  
869 simulated climate to the land surface model. To correct biases inherent in the climate model, in  
870 selected experiments we passed climate anomalies relative to a control simulation to the land  
871 model that were added to a standard baseline climatology based on contemporary observations. In  
872 simulations without this bias correction, raw simulated climate was passed directly from ModelE  
873 to LPJ-LMfire. Where bias correction was applied ModelE drifts towards warmer climate;  
874 simulations without bias correction drift towards colder climate. This effect was especially  
875 apparent in the high latitudes of the Northern Hemisphere, particularly over Asia. With bias  
876 correction, high latitude vegetation is dominated by tree plant functional types, while without it,

Deleted: strong

881 cold shrubs and arctic grasses are the predominant form of land cover. These results are  
882 characteristic of the well-known vegetation-albedo feedback that is important at high latitudes  
883 (Charney et al., 1977; Charney, 1975; Doughty et al., 2012, 2018; Pang et al., 2022; Stocker et al.,  
884 2013; Swann et al., 2010; Zeng et al., 2021).

885  
886 The effects of bias correction on precipitation were less apparent and confined to regional scale.  
887 We simulated a greater Indian summer monsoon season (JJAS) precipitation with bias correction  
888 (>1 mm/day), and a nominal increase of ~0.5 mm/day across east China, Africa, and the North  
889 American monsoon region. In other regions, the patterns of precipitation change were similar  
890 across all experiments except for Europe where drier conditions are simulated in summer (up to –  
891 1 mm/day) in simulations where bias correction was not applied.

892  
893 The high latitudes of the Northern Hemisphere were also the region with the largest disagreement  
894 between model and independent, multi-proxy temperature reconstructions. These comparisons  
895 also highlighted the important role of bias correction; experiments with correction were much more  
896 similar to reconstructions than those without. Simulations of the isotopic composition of  
897 precipitation ( $\delta^{18}\text{O}_p$ ) shows an excellent agreement with speleothem records with a pattern  
898 correlation greater than 0.8. However, the difference in the magnitude of model simulated  $\delta^{18}\text{O}_p$   
899 from proxies over various regions indicates an underestimation of relationship between surface  
900 temperature and  $\delta^{18}\text{O}_p$  variability (Henderson et al., 2006; Kurita et al., 2004). A global evaluation  
901 of model skill is hindered by the difference in the number of independent paleoclimate  
902 reconstructions available for different regions, particularly in north Asia where we see the greatest  
903 sensitivity of the coupled model system to the experimental setup. When examining modeled and  
904 reconstructed  $\delta^{18}\text{O}_p$ , in Europe, which is the region with the greatest number of records, we see a  
905 ~~robust~~ pattern correlation with lower RMS values as compared to other regions.

Deleted: stronger

906  
907 In this study, we confirmed the importance of the land surface for simulating paleoclimate, even  
908 for the late Holocene where land surface conditions were not as different from present as they were  
909 during, e.g., the last glacial cycle or even mid-Holocene (6ka). We demonstrated that asynchronous  
910 coupling can be a computationally inexpensive way of capturing land-atmosphere feedbacks and  
911 improving the fidelity of the simulated climate. We noted that correcting bias present in the climate

913 model is essential for simulating climate that is consistent with independent reconstructions,  
914 particularly for the high latitudes of the Northern Hemisphere. Future work with the coupled model  
915 system will include quantification of the influence of major volcanic eruptions for regional and  
916 global paleoclimate and the influence of past climate on the dynamics of complex civilizations in  
917 prehistory.

Deleted: (Singh et al., 2024, in preparation)

#### 918 **Code/Data availability**

919 Details to support the results in the manuscript is available as supplementary information is  
920 provided with the manuscript. GISS Model code snapshots are available at  
921 <https://simplex.giss.nasa.gov/snapshots/> (National Aeronautics and Space Administration, 2024),  
922 LPJ-LMfire (<https://zenodo.org/records/5831747>), and important codes, calculated diagnostics as  
923 well as other relevant details are available at zenodo repository  
924 (<https://doi.org/10.5281/zenodo.13626434>) (Singh et al., 2024). However, raw model outputs data  
925 and codes are available on request from author due to large data volume.

Deleted: F

926

#### 927 **Acknowledgements**

928 RS, KT, ANL and FL acknowledge support by the National Science Foundation under Grant No.  
929 ICER-1824770. ANL acknowledges institutional support from NASA GISS. Resources  
930 supporting this work were provided by the NASA High-End Computing (HEC) Program through  
931 the NASA Center for Climate Simulation (NCCS) at Goddard Space Flight Center and from the  
932 Department of Earth Sciences at The University of Hong Kong. The authors thank for their input  
933 through multiple discussions the project members and collaborators of the ICER-1824770 project,  
934 ‘Volcanism, Hydrology and Social Conflict: Lessons from Hellenistic and Roman-Era Egypt and  
935 Mesopotamia’. RS and FL acknowledge additional support from European Research Council grant  
936 agreement no. 951649 (4-OCEANS project).

Formatted: Font color: Text 1

937

#### 938 **Author’s contributions**

939 RS, KT and ANL identified the study period in consultation with the other authors and RS, AK,  
940 KT, ANL and JOK designed the asynchronous coupling framework. RS and AK implemented it  
941 and performed the simulations using NASA GISS ModelE and LPJ-LMfire models. IA and RR  
942 provided the essential technical support while implementing the framework. RS and RDR created  
943 the figures in close collaboration with KT, ANL. RS wrote the first draft of the manuscript and

946 RDR, KT, ANL, and JOK led the writing of subsequent drafts. All authors contributed to the  
947 interpretation of results and the drafting of the text.

948 **Competing interests**

949 The authors declare no competing interests.

950

951 **Short Summary**

952 This study presents and demonstrates an experimental framework for asynchronous land-  
953 atmosphere coupling using the NASA GISS ModelE and LPJ-LMfire models for the 2.5ka period.

954 This framework addresses the limitation of NASA ModelE, which does not have a fully dynamic  
955 vegetation model component. It also shows the role of model performance metrics, such as model  
956 bias and variability, and the simulated climate is evaluated against the multi-proxy paleoclimate  
957 reconstructions for the 2.5ka climate.

958

959 **References**

960 Aleinov, I. and Schmidt, G. A.: Water isotopes in the GISS ModelE land surface scheme, *Global  
961 and Planetary Change*, 51, 108–120, <https://doi.org/10.1016/j.gloplacha.2005.12.010>, 2006.

962 Baker, A., Hartmann, A., Duan, W., Hankin, S., Comas-Bru, L., Cuthbert, M. O., Treble, P. C.,  
963 Banner, J., Genty, D., Baldini, L. M., Bartolomé, M., Moreno, A., Pérez-Mejías, C., and Werner,  
964 M.: Global analysis reveals climatic controls on the oxygen isotope composition of cave drip  
965 water, *Nat Commun*, 10, 2984, <https://doi.org/10.1038/s41467-019-11027-w>, 2019.

966 Bauer, S. E., Tsigaridis, K., Faluvegi, G., Kelley, M., Lo, K. K., Miller, R. L., Nazarenko, L.,  
967 Schmidt, G. A., and Wu, J.: Historical (1850–2014) Aerosol Evolution and Role on Climate  
968 Forcing Using the GISS ModelE2.1 Contribution to CMIP6, *Journal of Advances in Modeling  
969 Earth Systems*, 12, e2019MS001978, <https://doi.org/10.1029/2019MS001978>, 2020.

970 Berger, A., Loutre, M. F., and Mélice, J. L.: Equatorial insolation: from precession harmonics to  
971 eccentricity frequencies, *Climate of the Past*, 2, 131–136, <https://doi.org/10.5194/cp-2-131-2006>,  
972 2006.

973 Betts, R. A.: Offset of the potential carbon sink from boreal forestation by decreases in surface  
974 albedo, *Nature*, 408, 187–190, <https://doi.org/10.1038/35041545>, 2000.

975 Bonan, G. B.: Forests and Climate Change: Forcings, Feedbacks, and the Climate Benefits of  
976 Forests, *Science*, 320, 1444–1449, <https://doi.org/10.1126/science.1155121>, 2008.

977 Bonan, G. B., Pollard, D., and Thompson, S. L.: Effects of boreal forest vegetation on global  
978 climate, *Nature*, 359, 716–718, <https://doi.org/10.1038/359716a0>, 1992.

979 Braconnot, P., Harrison, S. P., Kageyama, M., Bartlein, P. J., Masson-Delmotte, V., Abe-Ouchi,  
980 A., Otto-Bliesner, B., and Zhao, Y.: Evaluation of climate models using palaeoclimatic data,  
981 *Nature Clim Change*, 2, 417–424, <https://doi.org/10.1038/nclimate1456>, 2012.

982 Chandan, D. and Peltier, W. R.: African Humid Period Precipitation Sustained by Robust  
983 Vegetation, Soil, and Lake Feedbacks, *Geophysical Research Letters*, 47, e2020GL088728,  
984 <https://doi.org/10.1029/2020GL088728>, 2020.

985 Charney, J., Quirk, W. J., Chow, S., and Kornfield, J.: A Comparative Study of the Effects of  
986 Albedo Change on Drought in Semi-Arid Regions, *Journal of the Atmospheric Sciences*, 34,  
987 1366–1385, [https://doi.org/10.1175/1520-0469\(1977\)034<1366:ACSOTE>2.0.CO;2](https://doi.org/10.1175/1520-0469(1977)034<1366:ACSOTE>2.0.CO;2), 1977.

988 Charney, J. G.: Dynamics of deserts and drought in the Sahel, *Quarterly Journal of the Royal  
989 Meteorological Society*, 101, 193–202, <https://doi.org/10.1002/qj.49710142802>, 1975.

990 Claussen, M.: Modeling bio-geophysical feedback in the African and Indian monsoon region,  
991 *Climate Dynamics*, 13, 247–257, <https://doi.org/10.1007/s003820050164>, 1997.

992 Claussen\*, M.: Late Quaternary vegetation-climate feedbacks, *Climate of the Past*, 5, 203–216,  
993 <https://doi.org/10.5194/cp-5-203-2009>, 2009.

994 Collins, J. A., Prange, M., Caley, T., Gimeno, L., Beckmann, B., Mulitza, S., Skonieczny, C.,  
995 Roche, D., and Schefuß, E.: Rapid termination of the African Humid Period triggered by  
996 northern high-latitude cooling, *Nat Commun*, 8, 1372, <https://doi.org/10.1038/s41467-017-01454-y>, 2017.

998 Comas-Bru, L., Atsawawaranunt, K., Harrison, S., and members, S. working group: SISAL  
999 (Speleothem Isotopes Synthesis and AnaLysis Working Group) database version 2.0,  
1000 <https://doi.org/10.17864/1947.256>, 2020.

1001 Cox, P. M., Betts, R. A., Jones, C. D., Spall, S. A., and Totterdell, I. J.: Acceleration of global  
1002 warming due to carbon-cycle feedbacks in a coupled climate model, *Nature*, 408, 184–187,  
1003 <https://doi.org/10.1038/35041539>, 2000.

1004 Dallmeyer, A., Claussen, M., Lorenz, S. J., Sigl, M., Toohey, M., and Herzschuh, U.: Holocene  
1005 vegetation transitions and their climatic drivers in MPI-ESM1.2, *Climate of the Past*, 17, 2481–  
1006 2513, <https://doi.org/10.5194/cp-17-2481-2021>, 2021.

1007 Doherty, R., Kutzbach, J., Foley, J., and Pollard, D.: Fully coupled climate/dynamical vegetation  
1008 model simulations over Northern Africa during the mid-Holocene, *Climate Dynamics*, 16, 561–  
1009 573, <https://doi.org/10.1007/s003820000065>, 2000.

1010 Doughty, C. E., Loarie, S. R., and Field, C. B.: Theoretical Impact of Changing Albedo on  
1011 Precipitation at the Southernmost Boundary of the ITCZ in South America, *Earth Interactions*,  
1012 16, 1–14, <https://doi.org/10.1175/2012EI422.1>, 2012.

1013 Doughty, C. E., Santos-Andrade, P. E., Shenkin, A., Goldsmith, G. R., Bentley, L. P., Blonder,  
1014 B., Díaz, S., Salinas, N., Enquist, B. J., Martin, R. E., Asner, G. P., and Malhi, Y.: Tropical forest

1015 leaves may darken in response to climate change, *Nat Ecol Evol*, 2, 1918–1924,  
1016 <https://doi.org/10.1038/s41559-018-0716-y>, 2018.

1017 Eyring, V., Bony, S., Meehl, G. A., Senior, C. A., Stevens, B., Stouffer, R. J., and Taylor, K. E.:  
1018 Overview of the Coupled Model Intercomparison Project Phase 6 (CMIP6) experimental design  
1019 and organization, *Geoscientific Model Development*, 9, 1937–1958,  
1020 <https://doi.org/10.5194/gmd-9-1937-2016>, 2016.

1021 Fekete, B. M., Vörösmarty, C. J., and Lammers, R. B.: Scaling gridded river networks for  
1022 macroscale hydrology: Development, analysis, and control of error, *Water Resources Research*,  
1023 37, 1955–1967, <https://doi.org/10.1029/2001WR900024>, 2001.

1024 Gao, F., Morisette, J. T., Wolfe, R. E., Ederer, G., Pedelty, J., Masuoka, E., Myneni, R., Tan, B.,  
1025 and Nightingale, J.: An Algorithm to Produce Temporally and Spatially Continuous MODIS-  
1026 LAI Time Series, *IEEE Geoscience and Remote Sensing Letters*, 5, 60–64,  
1027 <https://doi.org/10.1109/LGRS.2007.907971>, 2008.

1028 Hamilton, D. S., Hantson, S., Scott, C. E., Kaplan, J. O., Pringle, K. J., Nieradzik, L. P., Rap, A.,  
1029 Folberth, G. A., Spracklen, D. V., and Carslaw, K. S.: Reassessment of pre-industrial fire  
1030 emissions strongly affects anthropogenic aerosol forcing, *Nat Commun*, 9, 3182,  
1031 <https://doi.org/10.1038/s41467-018-05592-9>, 2018.

1032 Harris, I., Osborn, T. J., Jones, P., and Lister, D.: Version 4 of the CRU TS monthly high-  
1033 resolution gridded multivariate climate dataset, *Sci Data*, 7, 109, <https://doi.org/10.1038/s41597-1034-020-0453-3>, 2020.

1035 Harrison, S. P., Bartlein, P. J., Izumi, K., Li, G., Annan, J., Hargreaves, J., Braconnot, P., and  
1036 Kageyama, M.: Evaluation of CMIP5 palaeo-simulations to improve climate projections, *Nature  
1037 Clim Change*, 5, 735–743, <https://doi.org/10.1038/nclimate2649>, 2015.

1038 Hartmann, A. and Baker, A.: Modelling karst vadose zone hydrology and its relevance for  
1039 paleoclimate reconstruction, *Earth-Science Reviews*, 172, 178–192,  
1040 <https://doi.org/10.1016/j.earscirev.2017.08.001>, 2017.

1041 Henderson, K., Laube, A., Gäggeler, H. W., Olivier, S., Papina, T., and Schwikowski, M.:  
1042 Temporal variations of accumulation and temperature during the past two centuries from  
1043 Belukha ice core, Siberian Altai, *Journal of Geophysical Research: Atmospheres*, 111,  
1044 <https://doi.org/10.1029/2005JD005819>, 2006.

1045 Hoesly, R. M., Smith, S. J., Feng, L., Klimont, Z., Janssens-Maenhout, G., Pitkanen, T., Seibert,  
1046 J. J., Vu, L., Andres, R. J., Bolt, R. M., Bond, T. C., Dawidowski, L., Kholod, N., Kurokawa, J.,  
1047 Li, M., Liu, L., Lu, Z., Moura, M. C. P., O'Rourke, P. R., and Zhang, Q.: Historical (1750–2014)  
1048 anthropogenic emissions of reactive gases and aerosols from the Community Emissions Data  
1049 System (CEDS), *Geoscientific Model Development*, 11, 369–408, <https://doi.org/10.5194/gmd-1050-11-369-2018>, 2018.

1051 Ito, G., Romanou, A., Kiang, N. Y., Faluvegi, G., Aleinov, I., Ruedy, R., Russell, G., Lerner, P.,  
1052 Kelley, M., and Lo, K.: Global Carbon Cycle and Climate Feedbacks in the NASA GISS

- 1053 ModelE2.1, *Journal of Advances in Modeling Earth Systems*, 12, e2019MS002030,  
1054 <https://doi.org/10.1029/2019MS002030>, 2020.
- 1055 Jahn, B., Schneider, R. R., Müller, P.-J., Donner, B., and Röhl, U.: Response of tropical African  
1056 and East Atlantic climates to orbital forcing over the last 1.7 Ma, *Geological Society, London,*  
1057 *Special Publications*, 247, 65–84, <https://doi.org/10.1144/GSL.SP.2005.247.01.04>, 2005.
- 1058 Kageyama, M., Braconnot, P., Harrison, S. P., Haywood, A. M., Jungclaus, J. H., Otto-Bliesner,  
1059 B. L., Peterschmitt, J.-Y., Abe-Ouchi, A., Albani, S., Bartlein, P. J., Brierley, C., Crucifix, M.,  
1060 Dolan, A., Fernandez-Donado, L., Fischer, H., Hopcroft, P. O., Ivanovic, R. F., Lambert, F.,  
1061 Lunt, D. J., Mahowald, N. M., Peltier, W. R., Phipps, S. J., Roche, D. M., Schmidt, G. A.,  
1062 Tarasov, L., Valdes, P. J., Zhang, Q., and Zhou, T.: The PMIP4 contribution to CMIP6 – Part 1:  
1063 Overview and over-arching analysis plan, *Geoscientific Model Development*, 11, 1033–1057,  
1064 <https://doi.org/10.5194/gmd-11-1033-2018>, 2018.
- 1065 Kaplan, J. O., Krumhardt, K. M., and Zimmermann, N. E.: The effects of land use and climate  
1066 change on the carbon cycle of Europe over the past 500 years, *Global Change Biology*, 18, 902–  
1067 914, <https://doi.org/10.1111/j.1365-2486.2011.02580.x>, 2012.
- 1068 Kaplan, J. O., Koch, A., and Vitali, R.: ARVE-Research/LPJ-LMfire: LPJ-LMfire (tropical  
1069 forest restoration), , <https://doi.org/10.5281/zenodo.5831747>, 2022.
- 1070 Kattge, J., Díaz, S., Lavorel, S., Prentice, I. C., Leadley, P., Bönisch, G., Garnier, E., Westoby,  
1071 M., Reich, P. B., Wright, I. J., Cornelissen, J. H. C., Violle, C., Harrison, S. P., Van BODEGOM,  
1072 P. M., Reichstein, M., Enquist, B. J., Soudzilovskaia, N. A., Ackerly, D. D., Anand, M., Atkin,  
1073 O., Bahn, M., Baker, T. R., Baldocchi, D., Bekker, R., Blanco, C. C., Blonder, B., Bond, W. J.,  
1074 Bradstock, R., Bunker, D. E., Casanoves, F., Cavender-Bares, J., Chambers, J. Q., Chapin Iii, F.  
1075 S., Chave, J., Coomes, D., Cornwell, W. K., Craine, J. M., Dobrin, B. H., Duarte, L., Durka, W.,  
1076 Elser, J., Esser, G., Estiarte, M., Fagan, W. F., Fang, J., Fernández-Méndez, F., Fidelis, A.,  
1077 Finegan, B., Flores, O., Ford, H., Frank, D., Freschet, G. T., Fyllas, N. M., Gallagher, R. V.,  
1078 Green, W. A., Gutierrez, A. G., Hickler, T., Higgins, S. I., Hodgson, J. G., Jalili, A., Jansen, S.,  
1079 Joly, C. A., Kerkhoff, A. J., Kirkup, D., Kitajima, K., Kleyer, M., Klotz, S., Knops, J. M. H.,  
1080 Kramer, K., Kühn, I., Kurokawa, H., Laughlin, D., Lee, T. D., Leishman, M., Lens, F., Lenz, T.,  
1081 Lewis, S. L., Lloyd, J., Llusià, J., Louault, F., Ma, S., Mahecha, M. D., Manning, P., Massad, T.,  
1082 Medlyn, B. E., Messier, J., Moles, A. T., Müller, S. C., Nadrowski, K., Naeem, S., Niinemets,  
1083 Ü., Nöllert, S., Nüske, A., Ogaya, R., Oleksyn, J., Onipchenko, V. G., Onoda, Y., Ordoñez, J.,  
1084 Overbeck, G., et al.: TRY – a global database of plant traits, *Global Change Biology*, 17, 2905–  
1085 2935, <https://doi.org/10.1111/j.1365-2486.2011.02451.x>, 2011.
- 1086 Kaufman, D., McKay, N., Routson, C., Erb, M., Dätwyler, C., Sommer, P. S., Heiri, O., and  
1087 Davis, B.: Holocene global mean surface temperature, a multi-method reconstruction approach,  
1088 *Sci Data*, 7, 201, <https://doi.org/10.1038/s41597-020-0530-7>, 2020.
- 1089 Kelley, M., Schmidt, G. A., Nazarenko, L. S., Bauer, S. E., Ruedy, R., Russell, G. L., Ackerman,  
1090 A. S., Aleinov, I., Bauer, M., Bleck, R., Canuto, V., Cesana, G., Cheng, Y., Clune, T. L., Cook,  
1091 B. I., Cruz, C. A., Del Genio, A. D., Elsaesser, G. S., Faluvegi, G., Kiang, N. Y., Kim, D., Lacis,  
1092 A. A., Leboissetier, A., LeGrande, A. N., Lo, K. K., Marshall, J., Matthews, E. E., McDermid,

1093 S., Mezuman, K., Miller, R. L., Murray, L. T., Oinas, V., Orbe, C., García-Pando, C. P.,  
1094 Perlwitz, J. P., Puma, M. J., Rind, D., Romanou, A., Shindell, D. T., Sun, S., Tausnev, N.,  
1095 Tsigaridis, K., Tselioudis, G., Weng, E., Wu, J., and Yao, M.-S.: GISS-E2.1: Configurations and  
1096 Climatology, *Journal of Advances in Modeling Earth Systems*, 12, e2019MS002025,  
1097 <https://doi.org/10.1029/2019MS002025>, 2020.

1098 Kim, Y., Moorcroft, P. R., Aleinov, I., Puma, M. J., and Kiang, N. Y.: Variability of phenology  
1099 and fluxes of water and carbon with observed and simulated soil moisture in the Ent Terrestrial  
1100 Biosphere Model (Ent TBM version 1.0.1.0.0), *Geoscientific Model Development*, 8, 3837–  
1101 3865, <https://doi.org/10.5194/gmd-8-3837-2015>, 2015.

1102 Kjellstroem, E., Strandberg, G., Brandefelt, J., Naeslund, J.-O., Smith, B., and Wohlfarth, B.:  
1103 Climate conditions in Sweden in a 100,000-year time perspective, 2009.

1104 Köhler, P., Nehrbass-Ahles, C., Schmitt, J., Stocker, T. F., and Fischer, H.: A 156 kyr smoothed  
1105 history of the atmospheric greenhouse gases CO<sub>2</sub>, CH<sub>4</sub>, and N<sub>2</sub>O and their radiative forcing,  
1106 *Earth System Science Data*, 9, 363–387, <https://doi.org/10.5194/essd-9-363-2017>, 2017.

1107 Kubatzki, C. and Claussen, M.: Simulation of the global bio-geophysical interactions during the  
1108 Last Glacial Maximum, *Climate Dynamics*, 14, 461–471,  
1109 <https://doi.org/10.1007/s003820050234>, 1998.

1110 Kurita, N., Yoshida, N., Inoue, G., and Chayanova, E. A.: Modern isotope climatology of Russia:  
1111 A first assessment, *Journal of Geophysical Research: Atmospheres*, 109,  
1112 <https://doi.org/10.1029/2003JD003404>, 2004.

1113 Lachniet, M. S.: Climatic and environmental controls on speleothem oxygen-isotope values,  
1114 *Quaternary Science Reviews*, 28, 412–432, <https://doi.org/10.1016/j.quascirev.2008.10.021>,  
1115 2009.

1116 Lamb, P. J.: Persistence of Subsaharan drought, *Nature*, 299, 46–48,  
1117 <https://doi.org/10.1038/299046a0>, 1982.

1118 LeGrande, A. N. and Schmidt, G. A.: Global gridded data set of the oxygen isotopic composition  
1119 in seawater, *Geophysical Research Letters*, 33, <https://doi.org/10.1029/2006GL026011>, 2006.

1120 Li, C.-F., Chytrý, M., Zelený, D., Chen, M.-Y., Chen, T.-Y., Chiou, C.-R., Hsia, Y.-J., Liu, H.-  
1121 Y., Yang, S.-Z., Yeh, C.-L., Wang, J.-C., Yu, C.-F., Lai, Y.-J., Chao, W.-C., and Hsieh, C.-F.:  
1122 Classification of Taiwan forest vegetation, *Applied Vegetation Science*, 16, 698–719,  
1123 <https://doi.org/10.1111/avsc.12025>, 2013.

1124 Louergue, L., Schilt, A., Spahni, R., Masson-Delmotte, V., Blunier, T., Lemieux, B., Barnola,  
1125 J.-M., Raynaud, D., Stocker, T. F., and Chappellaz, J.: Orbital and millennial-scale features of  
1126 atmospheric CH<sub>4</sub> over the past 800,000 years, *Nature*, 453, 383–386,  
1127 <https://doi.org/10.1038/nature06950>, 2008.

1128 Ludlow, F. and Manning, J. G.: Volcanic Eruptions, Veiled Suns, and Nile Failure in Egyptian  
1129 History: Integrating Hydroclimate into Understandings of Historical Change, in: *Climate Change*

1130 and Ancient Societies in Europe and the Near East: Diversity in Collapse and Resilience, edited  
1131 by: Erdkamp, P., Manning, J. G., and Verboven, K., Springer International Publishing, Cham,  
1132 301–320, [https://doi.org/10.1007/978-3-030-81103-7\\_10](https://doi.org/10.1007/978-3-030-81103-7_10), 2021.

1133 Magi, B. I.: Global Lightning Parameterization from CMIP5 Climate Model Output, *Journal of*  
1134 *Atmospheric and Oceanic Technology*, 32, 434–452, [https://doi.org/10.1175/JTECH-D-13-](https://doi.org/10.1175/JTECH-D-13-00261.1)  
1135 00261.1, 2015.

1136 Manning, J. G., Ludlow, F., Stine, A. R., Boos, W. R., Sigl, M., and Marlon, J. R.: Volcanic  
1137 suppression of Nile summer flooding triggers revolt and constrains interstate conflict in ancient  
1138 Egypt, *Nat Commun*, 8, 900, <https://doi.org/10.1038/s41467-017-00957-y>, 2017.

1139 Mikhail, A.: Ottoman Iceland: A Climate History, *Environmental History*, 20, 262–284,  
1140 <https://doi.org/10.1093/envhis/emv006>, 2015.

1141 Myneni, R. B., Hoffman, S., Knyazikhin, Y., Privette, J. L., Glassy, J., Tian, Y., Wang, Y., Song,  
1142 X., Zhang, Y., Smith, G. R., Lotsch, A., Friedl, M., Morisette, J. T., Votava, P., Nemani, R. R.,  
1143 and Running, S. W.: Global products of vegetation leaf area and fraction absorbed PAR from  
1144 year one of MODIS data, *Remote Sensing of Environment*, 83, 214–231,  
1145 [https://doi.org/10.1016/S0034-4257\(02\)00074-3](https://doi.org/10.1016/S0034-4257(02)00074-3), 2002.

1146 de Noblet, N., Braconnot, P., Joussaume, S., and Masson, V.: Sensitivity of simulated Asian and  
1147 African summer monsoons to orbitally induced variations in insolation 126, 115 and 6 kBP,  
1148 *Climate Dynamics*, 12, 589–603, <https://doi.org/10.1007/BF00216268>, 1996.

1149 Otto-Bliesner, B. L., Braconnot, P., Harrison, S. P., Lunt, D. J., Abe-Ouchi, A., Albani, S.,  
1150 Bartlein, P. J., Capron, E., Carlson, A. E., Dutton, A., Fischer, H., Goelzer, H., Govin, A.,  
1151 Haywood, A., Joos, F., LeGrande, A. N., Lipscomb, W. H., Lohmann, G., Mahowald, N.,  
1152 Nehrbass-Ahles, C., Pausata, F. S. R., Peterschmitt, J.-Y., Phipps, S. J., Renssen, H., and Zhang,  
1153 Q.: The PMIP4 contribution to CMIP6 – Part 2: Two interglacials, scientific objective and  
1154 experimental design for Holocene and Last Interglacial simulations, *Geoscientific Model*  
1155 *Development*, 10, 3979–4003, <https://doi.org/10.5194/gmd-10-3979-2017>, 2017.

1156 Pang, G., Chen, D., Wang, X., and Lai, H.-W.: Spatiotemporal variations of land surface albedo  
1157 and associated influencing factors on the Tibetan Plateau, *Science of The Total Environment*,  
1158 804, 150100, <https://doi.org/10.1016/j.scitotenv.2021.150100>, 2022.

1159 Pausata, F. S. R., Messori, G., and Zhang, Q.: Impacts of dust reduction on the northward  
1160 expansion of the African monsoon during the Green Sahara period, *Earth and Planetary Science*  
1161 *Letters*, 434, 298–307, <https://doi.org/10.1016/j.epsl.2015.11.049>, 2016.

1162 Petit-Maire, N. and Guo, Z. T.: Mid-Holocene climatic change and man in the present-day  
1163 Sahara desert, in: *Quaternary Deserts and Climatic Change*, CRC Press, 1998.

1164 Pfeiffer, M., Spessa, A., and Kaplan, J. O.: A model for global biomass burning in preindustrial  
1165 time: LPJ-LMfire (v1.0), *Geoscientific Model Development*, 6, 643–685,  
1166 <https://doi.org/10.5194/gmd-6-643-2013>, 2013.

- 1167 Rachmayani, R., Prange, M., and Schulz, M.: North African vegetation–precipitation feedback in  
1168 early and mid-Holocene climate simulations with CCSM3-DGVM, *Climate of the Past*, 11, 175–  
1169 185, <https://doi.org/10.5194/cp-11-175-2015>, 2015.
- 1170 Reale, O. and Dirmeyer, P.: Modeling the effects of vegetation on Mediterranean climate during  
1171 the Roman Classical Period: Part I: Climate history and model sensitivity, *Global and Planetary*  
1172 *Change*, 25, 163–184, [https://doi.org/10.1016/S0921-8181\(00\)00002-3](https://doi.org/10.1016/S0921-8181(00)00002-3), 2000.
- 1173 Schmidt, G. A.: Oxygen-18 variations in a global ocean model, *Geophysical Research Letters*,  
1174 25, 1201–1204, <https://doi.org/10.1029/98GL50866>, 1998.
- 1175 Schneider, R., Schmitt, J., Köhler, P., Joos, F., and Fischer, H.: A reconstruction of atmospheric  
1176 carbon dioxide and its stable carbon isotopic composition from the penultimate glacial maximum  
1177 to the last glacial inception, *Climate of the Past*, 9, 2507–2523, [https://doi.org/10.5194/cp-9-](https://doi.org/10.5194/cp-9-2507-2013)  
1178 [2507-2013](https://doi.org/10.5194/cp-9-2507-2013), 2013.
- 1179 Sha, L., Ait Brahim, Y., Wassenburg, J. A., Yin, J., Peros, M., Cruz, F. W., Cai, Y., Li, H., Du,  
1180 W., Zhang, H., Edwards, R. L., and Cheng, H.: How Far North Did the African Monsoon Fringe  
1181 Expand During the African Humid Period? Insights From Southwest Moroccan Speleothems,  
1182 *Geophysical Research Letters*, 46, 14093–14102, <https://doi.org/10.1029/2019GL084879>, 2019.
- 1183 Shanahan, T. M., McKay, N. P., Hughen, K. A., Overpeck, J. T., Otto-Bliesner, B., Heil, C. W.,  
1184 King, J., Scholz, C. A., and Peck, J.: The time-transgressive termination of the African Humid  
1185 Period, *Nature Geosci*, 8, 140–144, <https://doi.org/10.1038/ngeo2329>, 2015.
- 1186 Siegenthaler, U., Stocker, T. F., Monnin, E., Lüthi, D., Schwander, J., Stauffer, B., Raynaud, D.,  
1187 Barnola, J.-M., Fischer, H., Masson-Delmotte, V., and Jouzel, J.: Stable Carbon Cycle–Climate  
1188 Relationship During the Late Pleistocene, *Science*, 310, 1313–1317,  
1189 <https://doi.org/10.1126/science.1120130>, 2005.
- 1190 Simard, M., Pinto, N., Fisher, J. B., and Baccini, A.: Mapping forest canopy height globally with  
1191 spaceborne lidar, *Journal of Geophysical Research: Biogeosciences*, 116,  
1192 <https://doi.org/10.1029/2011JG001708>, 2011.
- 1193 Singh, R., Tsigaridis, K., LeGrande, A. N., Ludlow, F., and Manning, J. G.: Investigating  
1194 hydroclimatic impacts of the 168–158&thinsp;BCE volcanic quartet and their relevance to the  
1195 Nile River basin and Egyptian history, *Climate of the Past*, 19, 249–275,  
1196 <https://doi.org/10.5194/cp-19-249-2023>, 2023.
- 1197 Singh, R., Koch, A., LeGrande, A. N., Tsigaridis, K., Ramos, R. D., Ludlow, F., Aleinov, I.,  
1198 Ruedy, R., and Kaplan, J. O.: Modelling framework for asynchronous land-atmosphere coupling  
1199 using NASA GISS ModelE and LPJ-LMfire: Design, Application and Evaluation for the 2.5ka  
1200 period, <https://doi.org/10.5281/zenodo.13626434>, 2024.
- 1201 Sitch, S., Smith, B., Prentice, I. C., Arneth, A., Bondeau, A., Cramer, W., Kaplan, J. O., Levis,  
1202 S., Lucht, W., Sykes, M. T., Thonicke, K., and Venevsky, S.: Evaluation of ecosystem dynamics,  
1203 plant geography and terrestrial carbon cycling in the LPJ dynamic global vegetation model,  
1204 *Global Change Biology*, 9, 161–185, <https://doi.org/10.1046/j.1365-2486.2003.00569.x>, 2003.

1205 Stocker, T. F., Qin, D., Plattner, G.-K., Tignor, M. M. B., Allen, S. K., Boschung, J., Nauels, A.,  
1206 Xia, Y., Bex, V., Midgley, P. M., Alexander, L. V., Allen, S. K., Bindoff, N. L., Breon, F.-M.,  
1207 Church, J. A., Cubasch, U., Emori, S., Forster, P., Friedlingstein, P., Gillett, N., Gregory, J. M.,  
1208 Hartmann, D. L., Jansen, E., Kirtman, B., Knutti, R., Kumar Kanikicharla, K., Lemke, P.,  
1209 Marotzke, J., Masson-Delmotte, V., Meehl, G. A., Mokhov, I. I., Piao, S., Plattner, G.-K., Dahe,  
1210 Q., Ramaswamy, V., Randall, D., Rhein, M., Rojas, M., Sabine, C., Shindell, D., Stocker, T. F.,  
1211 Talley, L. D., Vaughan, D. G., Xie, S.-P., Allen, M. R., Boucher, O., Chambers, D., Hesselbjerg  
1212 Christensen, J., Ciais, P., Clark, P. U., Collins, M., Comiso, J. C., Vasconcellos de Menezes, V.,  
1213 Feely, R. A., Fichefet, T., Fiore, A. M., Flato, G., Fuglestedt, J., Hegerl, G., Hezel, P. J.,  
1214 Johnson, G. C., Kaser, G., Kattsov, V., Kennedy, J., Klein Tank, A. M. G., Le Quere, C., Myhre,  
1215 G., Osborn, T., Payne, A. J., Perlwitz, J., Power, S., Prather, M., Rintoul, S. R., Rogelj, J.,  
1216 Rusticucci, M., Schulz, M., Sedlacek, J., Stott, P. A., Sutton, R., Thorne, P. W., and Wuebbles,  
1217 D.: Climate Change 2013. The Physical Science Basis. Working Group I Contribution to the  
1218 Fifth Assessment Report of the Intergovernmental Panel on Climate Change - Abstract for  
1219 decision-makers; Changements climatiques 2013. Les elements scientifiques. Contribution du  
1220 groupe de travail I au cinquieme rapport d'evaluation du groupe d'experts intergouvernemental  
1221 sur l'evolution du CLIMAT - Resume a l'intention des decideurs, 2013.

1222 Strandberg, G., Brandefelt, J., Kjellstro" M, E., and Smith, B.: High-resolution regional  
1223 simulation of last glacial maximum climate in Europe, *Tellus A: Dynamic Meteorology and*  
1224 *Oceanography*, 63, 107–125, <https://doi.org/10.1111/j.1600-0870.2010.00485.x>, 2011.

1225 Strandberg, G., Kjellström, E., Poska, A., Wagner, S., Gaillard, M.-J., Trondman, A.-K., Mauri,  
1226 A., Davis, B. a. S., Kaplan, J. O., Birks, H. J. B., Bjune, A. E., Fyfe, R., Giesecke, T., Kalnina,  
1227 L., Kangur, M., van der Knaap, W. O., Kokfelt, U., Kuneš, P., Lata\l owa, M., Marquer, L.,  
1228 Mazier, F., Nielsen, A. B., Smith, B., Seppä, H., and Sugita, S.: Regional climate model  
1229 simulations for Europe at 6 and 0.2 k BP: sensitivity to changes in anthropogenic deforestation,  
1230 *Climate of the Past*, 10, 661–680, <https://doi.org/10.5194/cp-10-661-2014>, 2014a.

1231 Strandberg, G., Kjellström, E., Poska, A., Wagner, S., Gaillard, M.-J., Trondman, A.-K., Mauri,  
1232 A., Davis, B. a. S., Kaplan, J. O., Birks, H. J. B., Bjune, A. E., Fyfe, R., Giesecke, T., Kalnina,  
1233 L., Kangur, M., van der Knaap, W. O., Kokfelt, U., Kuneš, P., Lata\l owa, M., Marquer, L.,  
1234 Mazier, F., Nielsen, A. B., Smith, B., Seppä, H., and Sugita, S.: Regional climate model  
1235 simulations for Europe at 6 and 0.2 k BP: sensitivity to changes in anthropogenic deforestation,  
1236 *Climate of the Past*, 10, 661–680, <https://doi.org/10.5194/cp-10-661-2014>, 2014b.

1237 Swann, A. L., Fung, I. Y., Levis, S., Bonan, G. B., and Doney, S. C.: Changes in Arctic  
1238 vegetation amplify high-latitude warming through the greenhouse effect, *Proceedings of the*  
1239 *National Academy of Sciences*, 107, 1295–1300, <https://doi.org/10.1073/pnas.0913846107>,  
1240 2010.

1241 Texier, D., De Noblet, N., Harrison, S. P., Haxeltine, A., Jolly, D., Joussaume, S., Laarif, F.,  
1242 Prentice, I. C., and Tarasov, P.: Quantifying the role of biosphere-atmosphere feedbacks in  
1243 climate change: Coupled model simulations for 6000 years BP and comparison with palaeodata  
1244 for northern Eurasia and northern Africa, *Climate Dynamics*, 13, 865–882, 1997.

- 1245 Thomas, G. and Rowntree, P. R.: The Boreal Forests and Climate, *Quarterly Journal of the Royal*  
1246 *Meteorological Society*, 118, 469–497, <https://doi.org/10.1002/qj.49711850505>, 1992.
- 1247 Thompson, A. J., Tabor, C. R., Poulsen, C. J., and Skinner, C. B.: Water isotopic constraints on  
1248 the enhancement of the mid-Holocene West African monsoon, *Earth and Planetary Science*  
1249 *Letters*, 554, 116677, <https://doi.org/10.1016/j.epsl.2020.116677>, 2021.
- 1250 Thonicke, K., Spessa, A., Prentice, I. C., Harrison, S. P., Dong, L., and Carmona-Moreno, C.:  
1251 The influence of vegetation, fire spread and fire behaviour on biomass burning and trace gas  
1252 emissions: results from a process-based model, *Biogeosciences*, 7, 1991–2011,  
1253 <https://doi.org/10.5194/bg-7-1991-2010>, 2010.
- 1254 Tian, Y., Woodcock, C. E., Wang, Y., Privette, J. L., Shabanov, N. V., Zhou, L., Zhang, Y.,  
1255 Buermann, W., Dong, J., Veikkanen, B., Häme, T., Andersson, K., Ozdogan, M., Knyazikhin,  
1256 Y., and Myneni, R. B.: Multiscale analysis and validation of the MODIS LAI product: I.  
1257 Uncertainty assessment, *Remote Sensing of Environment*, 83, 414–430,  
1258 [https://doi.org/10.1016/S0034-4257\(02\)00047-0](https://doi.org/10.1016/S0034-4257(02)00047-0), 2002a.
- 1259 Tian, Y., Woodcock, C. E., Wang, Y., Privette, J. L., Shabanov, N. V., Zhou, L., Zhang, Y.,  
1260 Buermann, W., Dong, J., Veikkanen, B., Häme, T., Andersson, K., Ozdogan, M., Knyazikhin,  
1261 Y., and Myneni, R. B.: Multiscale analysis and validation of the MODIS LAI product: II.  
1262 Sampling strategy, *Remote Sensing of Environment*, 83, 431–441,  
1263 [https://doi.org/10.1016/S0034-4257\(02\)00058-5](https://doi.org/10.1016/S0034-4257(02)00058-5), 2002b.
- 1264 Tierney, J. E., Pausata, F. S. R., and deMenocal, P. B.: Rainfall regimes of the Green Sahara,  
1265 *Science Advances*, 3, e1601503, <https://doi.org/10.1126/sciadv.1601503>, 2017.
- 1266 Tiwari, S., Ramos, R. D., Pausata, F. S. R., LeGrande, A. N., Griffiths, M. L., Beltrami, H.,  
1267 Wainer, I., de Vernal, A., Litchmore, D. T., Chandan, D., Peltier, W. R., and Tabor, C. R.: On  
1268 the Remote Impacts of Mid-Holocene Saharan Vegetation on South American Hydroclimate: A  
1269 Modeling Intercomparison, *Geophysical Research Letters*, 50, e2022GL101974,  
1270 <https://doi.org/10.1029/2022GL101974>, 2023.
- 1271 Velasquez, P., Kaplan, J. O., Messmer, M., Ludwig, P., and Raible, C. C.: The role of land cover  
1272 in the climate of glacial Europe, *Climate of the Past*, 17, 1161–1180, [https://doi.org/10.5194/cp-](https://doi.org/10.5194/cp-17-1161-2021)  
1273 [17-1161-2021](https://doi.org/10.5194/cp-17-1161-2021), 2021.
- 1274 Yang, W., Tan, B., Huang, D., Rautiainen, M., Shabanov, N. V., Wang, Y., Privette, J. L.,  
1275 Huemmrich, K. F., Fensholt, R., Sandholt, I., Weiss, M., Ahl, D. E., Gower, S. T., Nemani, R.  
1276 R., Knyazikhin, Y., and Myneni, R. B.: MODIS leaf area index products: from validation to  
1277 algorithm improvement, *IEEE Transactions on Geoscience and Remote Sensing*, 44, 1885–1898,  
1278 <https://doi.org/10.1109/TGRS.2006.871215>, 2006.
- 1279 Zeng, Z., Wang, D., Yang, L., Wu, J., Ziegler, A. D., Liu, M., Ciais, P., Searchinger, T. D.,  
1280 Yang, Z.-L., Chen, D., Chen, A., Li, L. Z. X., Piao, S., Taylor, D., Cai, X., Pan, M., Peng, L.,  
1281 Lin, P., Gower, D., Feng, Y., Zheng, C., Guan, K., Lian, X., Wang, T., Wang, L., Jeong, S.-J.,  
1282 Wei, Z., Sheffield, J., Caylor, K., and Wood, E. F.: Deforestation-induced warming over tropical

1283 mountain regions regulated by elevation, *Nat. Geosci.*, 14, 23–29,  
1284 <https://doi.org/10.1038/s41561-020-00666-0>, 2021.

1285

